energies

MDPI

Review

Rare Earth Borohydrides—Crystal Structures and Thermal Properties

Christoph Frommen [1], Magnus H. Sørby [1], Michael Heere [1,2], Terry D. Humphries [3], Jørn E. Olsen [1] and Bjørn C. Hauback [1,*]

[1] Institute for Energy Technology, Physics Department, P.O. Box 40, NO-2027 Kjeller, Norway; christoph.frommen@ife.no (C.F.); magnuss@ife.no (M.H.S.); michael.heere@kit.edu (M.H.); jorneirikolsen@hotmail.com (J.E.O.)
[2] Research Neutron Source Munich (FRM2) and Karlsruhe Institute of Technology (KIT), Institute for Applied Materials—Energy Storage Systems (IAM-ESS), 76344 Eggenstein, Germany
[3] Department of Physics and Astronomy, Fuels and Energy Technology Institute, Curtin University, GPO Box U1987, Perth 6845, Australia; terry.humphries@curtin.edu.au
* Correspondence: bjorn.hauback@ife.no; Tel.: +47-974-08-844

Received: 3 November 2017; Accepted: 4 December 2017; Published: 12 December 2017

Abstract: Rare earth (*RE*) borohydrides have received considerable attention during the past ten years as possible hydrogen storage materials due to their relatively high gravimetric hydrogen density. This review illustrates the rich chemistry, structural diversity and thermal properties of borohydrides containing *RE* elements. In addition, it highlights the decomposition and rehydrogenation properties of composites containing *RE*-borohydrides, light-weight metal borohydrides such as $LiBH_4$ and additives such as LiH.

Keywords: borohydrides; complex metal hydrides; rare earth; hydrogen storage; crystal structure; thermal properties; composites; reversibility

1. Introduction

Metal borohydrides are being intensively studied as potential hydrogen and thermal energy storage materials [1–7] as well as solid state electrolytes [8–11]. Alkali and alkaline earth borohydrides such as $LiBH_4$ and $Mg(BH_4)_2$ are of great interest due to their high gravimetric hydrogen storage capacity. Unfortunately, their decomposition temperatures are too high and rehydrogenation only occurs under severe conditions as a result of the strong ionic interaction between the metal cation and the BH_4^- anion. In contrast, complexes containing transition metal cations are too unstable with decomposition temperatures below or slightly above room temperature. In recent years, a correlation between the thermodynamic stability (decomposition temperature) and the Pauling electronegativity of the metal cation has been established [12]. According to reference [12] the hydrogen desorption temperature decreases with increasing electronegativity of the metal. This result suggests that the charge transfer from the metal cation to the BH_4^- anion is responsible for the stability of the metal borohydride. It has become apparent that borohydrides with Pauling electronegativities larger than 1.4 are too unstable for use in hydrogen storage applications. Tuning the thermodynamic properties of borohydrides has been attempted by the combination of different metal cations to form double-cation metal borohydrides $M^{n+}M^{m+}(BH_4)_{(n+m)}$ (M^{n+} = Li^+, Na^+, K^+; M^{m+} = transition metal cation). The search for new possible candidates for hydrogen storage applications has stimulated interest in materials containing rare earth (*RE*) metal cations. The gravimetric hydrogen storage density of monometallic *RE*-borohydrides ranges from 9.1 wt % H_2 for $Y(BH_4)_3$ to 5.6 wt % H_2 for $Yb(BH_4)_3$, respectively, and their thermodynamic stability is expected to lie between those of the alkali and transition metals. Compared to alkali or alkaline-earth borohydrides such as $LiBH_4$ (18.5 wt % H_2) or

$Mg(BH_4)_2$ (14.9 wt % H_2), *RE*-borohydrides possess lower gravimetric hydrogen density. However, they are able to release a major amount of hydrogen between 200 and 300 °C, which is significantly lower than for $LiBH_4$ or $Mg(BH_4)_2$. As a result, a large number of novel *RE*-borohydrides have been synthesized and more than 50 papers have been published since 2008. The majority of publications are focused on the synthesis and structural characterization of the compounds and several extensive reviews already exist [1,4,7]. In contrast, less information is available about the thermal properties and rehydrogenation behavior of pure *RE*-borohydrides or as part of composites.

The current review article presents the state of the art on the crystal structure and thermodynamic properties of pure *RE*-borohydrides. In addition, we elucidate the thermal decomposition and rehydrogenation behavior of *RE*-borohydrides in composite mixtures containing $LiBH_4$ and additives such as LiH. The layout is as follows: Section 2 details commonly applied synthesis procedures for *RE*-borohydrides; Section 3 summarizes the crystal structures of mono-, di- and trimetallic borohydrides containing rare earth elements; Section 4 presents the thermal properties of *RE*-borohydrides starting from monometallic and halide substituted compounds, followed by composite mixtures containing *RE*-borohydrides, $LiBH_4$ and LiH. This is the first time that the state of the art for the decomposition and rehydrogenation behavior of composites containing *RE*-borohydrides has been summarized in literature.

2. Synthesis of Metal Borohydrides

The synthesis of borohydrides is mostly carried out by either solvent-based methods or by mechanochemistry. Both approaches offer distinct advantages, but also suffer from certain drawbacks. The first solvent-based synthesis of a metal borohydride, $Mg(BH_4)_2$, was reported by Wiberg and Bauer in 1950 and was based on the reaction of diethylmagnesium, $Mg(CH_2CH_3)_2$, and diborane, B_2H_6, in ether [13]. However, the authors were not aware of a stable solvent adduct that was formed under the experimental conditions described in their paper. A direct synthesis route for $Mg(BH_4)_2$ from the elements was described in a German patent from 1958 [14]. However, attempts to reproduce the procedure were not successful in obtaining sufficiently high yields and it was impossible to separate the product from the rest of the reaction mixture by solvent extraction [15]. In order to circumvent the high reactivity of diborane towards air and moisture and its inherent toxicity, Koester [16] developed a synthesis method in 1957 based on the reaction of the respective metal hydride with N-alkylborazanes instead of diborane. This method has since then been successfully adapted to substitute diborane by safer and easier to handle borane complexes such as triethylamine borane, $(CH_3CH_2)_3NBH_3$, or dimethylsulfide borane, $(CH_3)_2SBH_3$. The underlying principal of each of the synthesis methods named above, is that a metal hydride or metal alkyl reacts with a borane donor anion. This leads to the formation of a solvated metal borohydride complex, which in turn requires further thermal treatment in order to obtain the solvent-free product [15,17]. A major risk of this synthesis method lies in the decomposition of the borohydride during thermal treatment and solvent removal. The same risk also exists for the metathesis reactions between an alkali borohydride (mostly $LiBH_4$) and a metal chloride carried out in organic solvents such as ether or toluene. However, this strategy has been successful in obtaining the desired borohydride, e.g. in the case of $Al(BH_4)_3$ and other compounds according to Equation (1):

$$3LiBH_{4\,(s)} + AlCl_{3\,(s)} \rightarrow Al(BH_4)_{3\,(l)} + 3LiCl_{\,(s)} \tag{1}$$

The use of a weakly coordinating solvent that selectively dissolves the borohydride then allows for the removal of the metal halide by solvent extraction. The separation of the borohydride from the metal halide by-product is the major advantage of the solvent-based approach and allows for structural and thermal studies on the pure and halide-free materials.

Mechanochemistry is the most commonly applied approach for the preparation of borohydrides. High-energy ball milling can incite a chemical metathesis reaction between an alkali borohydride (Li, Na, K) and the respective metal chloride in the solid state. $LiBH_4$ has so far proven to be the most efficient precursor for these reactions, while attempts with other metal borohydrides, e.g., $NaBH_4$, generally offers poor yields at most [9,18–31].

The high energy impaction between the milling balls and the powder causes a continuous fracturing and welding process that can induce grain refinement, produce fresh and reactive surfaces and provide nucleation centers for the chemical growth of reaction products. The major advantage of the ball milling method lies in the possibility to obtain metastable compounds at ambient conditions as the process proceeds far away from thermal equilibrium. In addition, ball milling provides access to more complicated bi-/trimetallic borohydrides in contrast to the solvent-based approach, which typically only yields the monometallic compounds. However, special care has to be taken in order to avoid decomposition of the product during ball milling or the formation of halide-substituted compounds. Such unwanted reactions can be suppressed by adding sufficient pauses to the milling protocol and by avoiding prolonged milling times. The metathesis reaction involving stoichiometric ratios of a trivalent *RE* metal chloride and lithium borohydride results in the formation of a mono- or bimetallic *RE*-borohydride, or a chloride substituted *RE*-borohydride, $LiRE(BH_4)_3Cl$ (Table 1), according to Equations (2)–(4):

$$RECl_3 + 3LiBH_4 \rightarrow RE(BH_4)_3 + 3LiCl \tag{2}$$

$$RECl_3 + 4LiBH_4 \rightarrow LiRE(BH_4)_4 + 3LiCl \tag{3}$$

$$RECl_3 + 3LiBH_4 \rightarrow LiRE(BH_4)_3Cl + 2LiCl \tag{4}$$

Unfortunately, the mechanochemical metathesis approach suffers from three major drawbacks. Firstly, the reaction products after ball milling are often not very crystalline and therefore require additional careful heat treatment in order to heal out structure defects and improve their crystallinity. Secondly, the product mixture always consists of the borohydride and a metal halide, the latter simply being "dead weight", thereby effectively lowering the gravimetric hydrogen capacity. Finally, the metal halide may influence the chemical and physical properties of the borohydride and may affect its decomposition temperature or modify the decomposition pathway.

In order to avoid the drawbacks of the mechanochemical metathesis approach and to allow for halide-free products to be obtained, wet-chemical methods have been developed. They are based on the selective dissolution of the *RE*-borohydride in an organic solvent such as diethylether, toluene or dimethyl sulfide, followed by removal of the unwanted by-products (e.g., LiCl) through filtering, and careful drying of the solvated product *in vacuo*. The interested reader is referred to reference [1] for a more detailed description of the various synthesis procedures for metal borohydrides and their derivatives.

Table 1. Structure types for binary and ternary lithium rare earth borohydrides formed by metathesis reactions between $LiBH_4$ and $RECl_3$.

***RE* Ion**	**Ion Radius [Å]**	**Li*RE*(BH_4)$_4$ ($CuAuCl_4$)**	**α-*RE*(BH_4)$_3$ (ReO_3)**	**β-*RE*(BH_4)$_3$ (ReO_3)**	**Li*RE*(BH_4)$_3$Cl (Spinel)**
Sc^{3+}	0.745	X			
Y^{3+}	0.90		X	X	
La^{3+}	1.172				X
Ce^{3+}	1.15			X	X
Pr^{3+}	1.13		X	X	X
Nd^{3+}	1.123				X
Sm^{3+}	1.098		X	X	X
Gd^{3+}	1.078		X		X
Tb^{3+}	1.063		X		
Dy^{3+}	1.052		X		
Ho^{3+}	1.041		X	X	
Er^{3+}	1.03		X	X	
Yb^{3+}	1.008	X	X	X	
Lu^{3+}	1.001	X			

3. Crystal Structures

3.1. Monometallic RE-Borohydrides

All of the known monometallic *RE*-borohydrides are summarized in Table 2 and their crystal structures are discussed below.

3.1.1. Distorted ReO_3-Type (α-$RE(BH_4)_3$)

The distorted ReO_3-type structure (space group $Pa\bar{3}$) was suggested for $Y(BH_4)_3$, $Gd(BH_4)_3$ and $Dy(BH_4)_3$ from laboratory powder X-ray diffraction (PXD) data by Sato et al. [18]. The RE^{3+} ions form a pseudo-cube with BH_4^- approximately at the center of the pseudo-cube edges (Figure 1). $Y(BH_4)_3$ was further investigated as a hydride and deuteride with high-resolution synchrotron radiation powder X-ray diffraction (SR-PXD) and powder neutron diffraction (PND), respectively. However, the deuterated PND sample contained highly neutron-absorbing natural boron and they were thus unable to refine the atomic positions of boron or deuterium. Frommen et al. [21] performed combined SR-PXD and PND investigation on a double-isotope substituted sample, $Y(^{11}BD_4)_3$. Structure refinements revealed a significant distortion compared to the undistorted ReO_3-type structure (see Section 3.1.2). The B-Y-B angle is for instance 160.9° compared to 180° for an undistorted ReO_3-structure and the D-B-D angles take values between 103 and 115° (ideal value 109.5°).

The same structure type has been reported from SR-PXD data for $Sm(BH_4)_3$, $Gd(BH_4)_3$, $Tb(BH_4)_3$, $Dy(BH_4)_3$, $Er(BH_4)_3$, $Ho(BH_4)_3$, $Tm(BH_4)_3$, $Yb(BH_4)_3$ [19,29,30,32,33]. Due to the challenges with extreme neutron absorption in Sm, Dy and Gd, in addition to the general problem with absorption in natural boron and incoherent scattering from H, these phases have not been investigated by PND and thus accurate positions for B and H have not been obtained. The unit cell parameters obtained from PXD show a near linear dependence on the radius of the RE^{3+} cation (Figure 2).

Table 2. Monometallic rare earth borohydrides. RT = room temperature; HT = high temperature polymorph; meta = metastable.

Cation	Polymorph	Hydrogen Capacity (wt %)	Stability	Crystal System	Space Group	Structure Type	Ref.
Y^{3+}	α-$Y(BH_4)_3$ β-$Y(BH_4)_3$	9.1	RT RT, HT	Cubic Cubic	$Pa\bar{3}$ $Fm\bar{3}c$	Distorted ReO_3 ReO_3	[18] [21]
La^{3+}	$La(BH_4)_3$	6.6	RT	Trigonal	$R\bar{3}c$	Distorted ReO_3	[34]
Ce^{3+}	$Ce(BH_4)_3$	6.6	RT	Cubic Trigonal	$Fm\bar{3}c$ $R\bar{3}c$	ReO_3 Distored ReO_3	[34] [34]
Pr^{3+}	$Pr(BH_4)_3$	6.5	RT	Cubic	$Pa\bar{3}$ $Pm\bar{3}m$	Distorted ReO_3 ReO_3	[30]
Sm^{2+}	o-$Sm(BH_4)_2$	4.5	~500 K	Orthorhombic	$Pbcn$	ort-$Sr(BH_4)_2$	[19,27]
Sm^{3+}	α-$Sm(BH_4)_3$ β-$Sm(BH_4)_3$	6.2	RT RT	Cubic Cubic	$Pa\bar{3}$ $Pm\bar{3}m$	Distorted ReO_3 ReO_3	[19] [19]
Eu^{2+}	o-$Eu(BH_4)_2$ t-$Eu(BH_4)_2$ c-$Eu(BH_4)_2$	4.4	~430 K >668 K >668 K	Orthorhombic Tetragonal Cubic	$Pbcn$ $P4_12_12$ $Pm\bar{3}m$	orthorombic $Sr(BH_4)_2$ tetragonal $Sr(BH_4)_2$ cubic $Sr(BH_4)_2$	[27] [35] [35]
Gd^{3+}	$Gd(BH_4)_3$	6.0	RT	Cubic	$Pa\bar{3}$	Distorted ReO_3	[18,19]
Tb^{3+}	$Tb(BH_4)_3$	5.9	RT	Cubic	$Pa\bar{3}$	Distorted ReO_3	[19]
Dy^{3+}	$Dy(BH_4)_3$	5.8	RT	Cubic	$Pa\bar{3}$	Distorted ReO_3	[18]
Ho^{3+}	α-$Ho(BH_4)_3$ β-$Ho(BH_4)_3$	5.8	RT RT	Cubic Cubic	$Pa\bar{3}$ $Fm\bar{3}c$	Distorted ReO_3 ReO_3	[32] [32]
Er^{3+}	α-$Er(BH_4)_3$ β-$Er(BH_4)_3$	5.7	RT RT	Cubic Cubic	$Pa\bar{3}$ $Pm\bar{3}m$	Distorted ReO_3 ReO_3	[19] [19]
Tm^{3+}	α-$Tm(BH_4)_3$	5.7		Cubic	$Pa\bar{3}$	Distorted ReO_3	[33]
Yb^{2+}	α-$Yb(BH_4)_2$ β-$Yb(BH_4)_2$ γ-$Yb(BH_4)_2$	4.0	RT >523 K 473–573 K	Orthorhombic Tetragonal Orthorhombic	$F2dd$ $P\bar{4}$ $Pbca$	α-$Ca(BH_4)_2$ β-$Ca(BH_4)_2$ γ-$Ca(BH_4)_2$	[1] [29] [29]
Yb^{3+}	α-$Yb(BH_4)_3$ β-$Yb(BH_4)_3$	5.6	RT RT, meta	Cubic Cubic	$Pa\bar{3}$ $Pm\bar{3}m$	Distorted ReO_3 ReO_3	[29] [29]

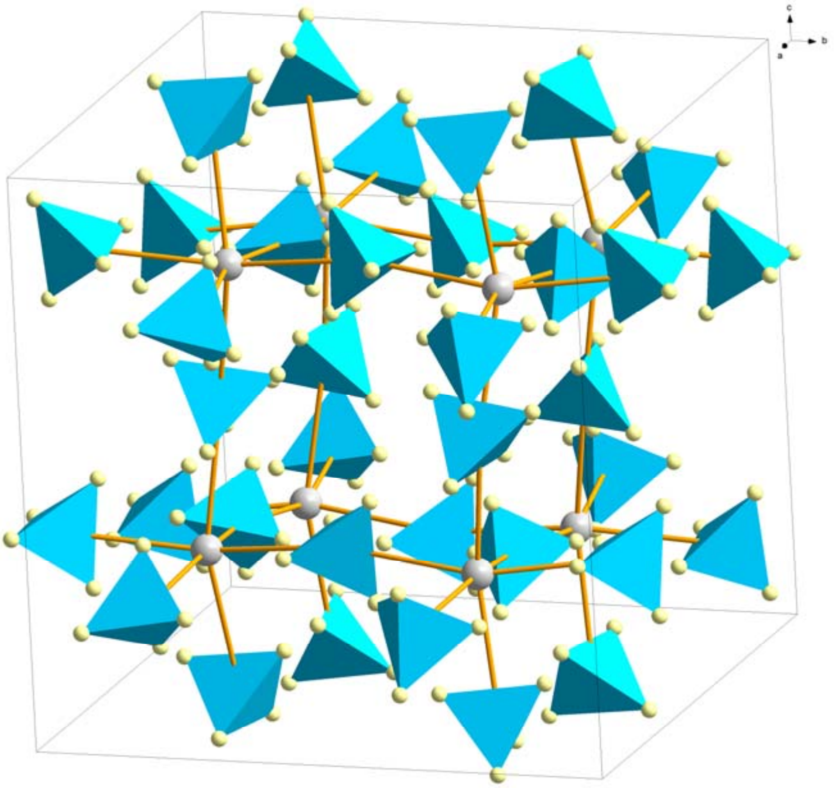

Figure 1. The crystal structure of α-*RE*$(BH_4)_3$, space group *Pa*$\overline{3}$. The pseudo-cubic arrangement of RE^{3+} (grey spheres) and their octahedral coordination of 6 BH_4^- (blue tetrahedra) are outlined.

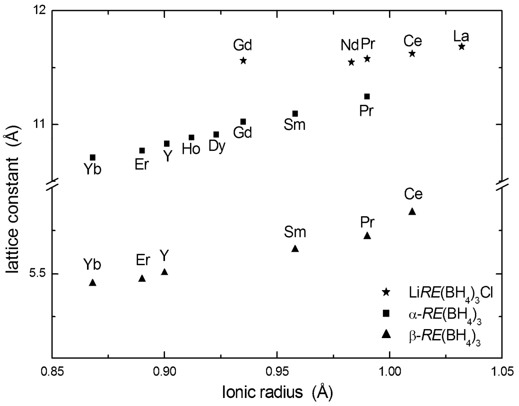

Figure 2. Reported unit cell parameters for α-*RE*$(BH_4)_3$, β-*RE*$(BH_4)_3$, Li*RE*$(BH_4)_3Cl$ as a function of ionic radii of the RE^{3+} ions. The unit cell parameter for the β-Y$(BH_4)_3$ superstructure is divided by 2 to be comparable with the other β-*RE*$(BH_4)_3$ phases.

3.1.2. ReO_3-Type (β-*RE*$(BH_4)_3$)

Differential scanning calorimetry (DSC) measurements of $Y(BH_4)_3$ indicated a structural phase transition between 199 and 488 °C [21]. The high-temperature phase was found to be metastable at ambient temperature in samples that were quenched after annealing above the phase transition temperature [21,22]. PXD data of the quenched material indicated a primitive cubic unit cell with a = 5.4547 Å and Rietveld refinements of the data showed excellent agreement with a regular ReO_3-type structure (space group *Pm*$\overline{3}$*m*). Y is positioned in the unit cell corners, octahedrally coordinated by BH_4^- at the center of each unit cell edge (Figure 3). In the reported space group symmetry, the BH_4^- units are disordered with 8 half-occupied D sites around each boron [22]. Further investigation of a

$Y(^{11}BD_4)_2$ sample by PND measurement indicated a face-centered cubic unit cell with doubled unit cell axes (space group $Fm\overline{3}c$, a = 11.0086 Å). Rietveld refinement with this data yielded a model with identical Y and B distribution compared to the structure refined from PXD data alone, although the BH_4^- ions are now deemed to have an ordered orientation and are rotated by 90° relative to their closest neighbors in both the *a*, *b* and *c*-directions [21] (Figure 4). The strongest superstructure peak from the BH_4^- ordering in the PXD data has about 0.3% of the intensity of the strongest peak and is therefore virtually impossible to detect (Figure 5). In contrast, the superstructure peak with Miller index 531 is the strongest Bragg peak in the PND data (Figure 6).

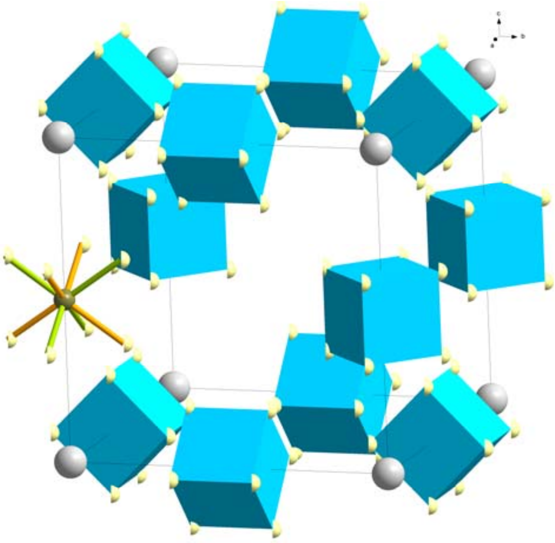

Figure 3. Crystal structure of β-*RE*$(BH_4)_3$, space group $Pm\overline{3}m$. The boron atoms have a cubic coordination (blue) of half-occupied hydrogen sites (yellow half-spheres). This represent two different orientations of the BH_4-tetrahdra as outlined for one boron where green and orange bonds represent two different BH_4^- orientations.

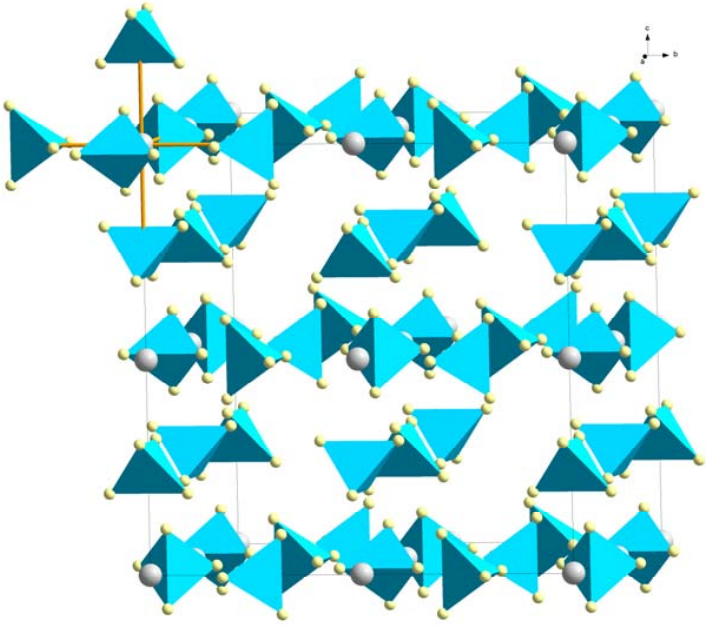

Figure 4. Crystal structure of β-$Y(BH_4)_3$, space group $Fm\overline{3}c$. The octahedral coordination of one Y^{3+} (white) is outlined. Note the alternating orientations of the BH_4^- ions (light blue) along the three axes of the unit cell.

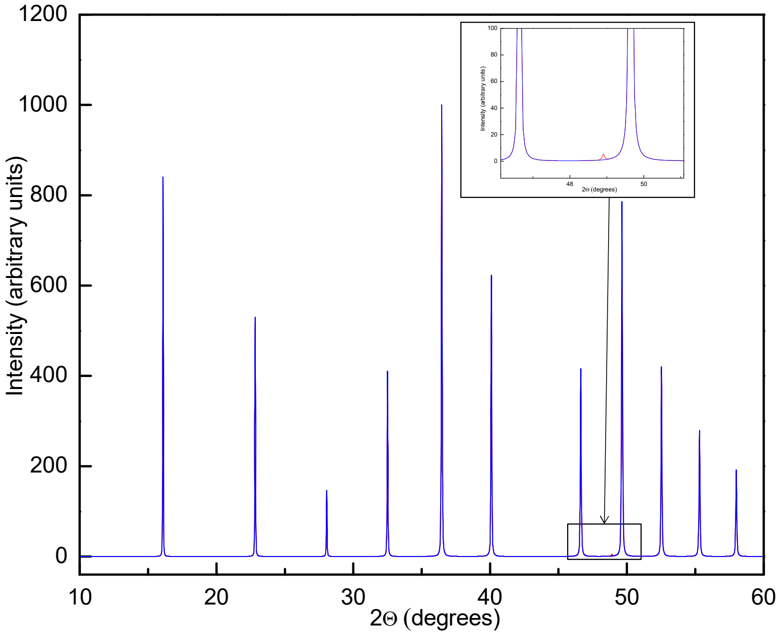

Figure 5. Simulated powder X-ray diffraction (PXD) data ($CuK_{\alpha 1}$) for β-$Y(BH_4)_3$ with disordered structure and space group *Pm*$\overline{3}$*m* (blue curve) and a ordered structure with doubled unit cell edges and space group *Fm*$\overline{3}$*c* (red curve). The red curve is mostly not visible due almost perfect overlap with the blue curve. The strongest superstructure peak 531 is shown inset and barely visible even in the noise-free simulated data.

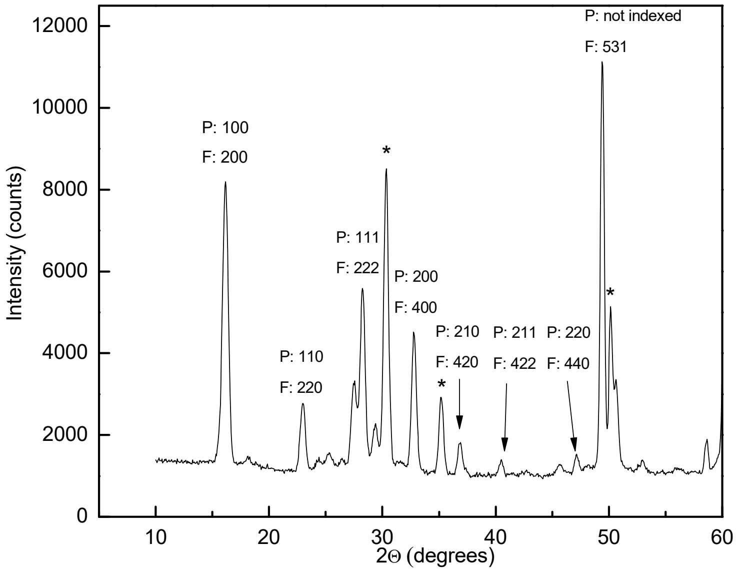

Figure 6. Powder neutron diffraction (PND) data for β-$Y(^{11}BD_4)_3$. Miller indices for the small disordered unit cell (P) and the large ordered unit cell (F) are indicated. LiCl peaks are marked with * and unindexed peaks are from $Li^{11}BD_4$. Note the high intensity of the superstructure peak ("F: 531"). λ = 1.5558 Å.

SR-PXD measurements have revealed that β-*RE*$(BH_4)_3$ modifications also exist for $Ce(BH_4)_3$, $Pr(BH_4)_3$, $Sm(BH_4)_3$, $Ho(BH_4)_3$, $Er(BH_4)_3$ and $Yb(BH_4)_3$ [19,29,30,32,34]. Due to the chemical similarity of these *RE* ions and Y^{3+}, it seems likely that these phases take structures with ordered BH_4^- orientations. However, due to lack of experimental verification, most of these structures were reported in the simplest model consistent with the PXD data, i.e., primitive cubic ReO_3-type unit cells (space group $Pm\bar{3}m$) with disordered BH_4^- units (Table 2). The correlation between the unit cell parameters and the cation radii are shown in Figure 2.

3.1.3. Alkaline Earth Borohydride-Types

Sm, Eu, Tm and Yb can exist in the 2+ oxidation state and divalent borohydrides have been reported for all of them except Tm. Sm^{2+} and Eu^{2+} have ionic radii of 1.2 Å and 1.17 Å, respectively, which are similar to that of Sr^{2+} (1.18 Å). $Sm(BH_4)_2$ [19,27] and $Eu(BH_4)_2$ [27,35] have been reported to crystallize in the same structure type as the room temperature (RT) modification of $Sr(BH_4)_2$ [35] (space group *Pbcn*, α-PbO_2 type structure). The RE^{2+} is octahedrally coordinated by $6BH_4^-$, with the $RE(BH_4)_6$ octahedra sharing all six vertices and two edges with other $RE(BH_4)_6$ octahedra, creating zigzag chains along the *c*-axis. Each chain is again linked by vertices to four other chains. The borohydride tetrahedron is surrounded by three M^{2+} ions and forms nearly perfect trigonal planar coordination.

$Eu(BH_4)_2$ forms two additional polymorphs at higher temperatures; one tetragonal (space group $P4_12_12$, superstructure of high temperature (HT)-ZrO_2-type) and one cubic (space group $Fm\bar{3}c$, CaF_2-related). Both are isostructural to HT polymorphs of $Sr(BH_4)_2$ [35]. Both HT polymorphs have 8-coordinated Eu^{2+}. The tetragonal $Eu(BH_4)_2$ polymorph can be regarded as a distorted version of the CaF_2-type polymorph. Thus, both consist of distorted (tetragonal polymorph) or regular (cubic polymorph) $Eu(BH_4)_8$ cubes that share all edges with other $Eu(BH_4)_8$ cubes.

Yb^{2+} has a similar ionic radius to Ca^{2+} (1.16 Å and 1.18 Å, respectively) and the three reported $Yb(BH_4)_2$ modifications are isostructural to known $Ca(BH_4)_2$ phases. An orthorhombic α-$Yb(BH_4)_2$ (space group *F*2*dd*), which is isostructural to α-$Ca(BH_4)_2$ is reported to be the stable polymorph at ambient temperature [1]. The two high-temperature polymorphs are isostructural to β-$Ca(BH_4)_2$ (space group $P\bar{4}$) and γ-$Ca(BH_4)_2$ (space group *Pbca*) [29]. Both of these HT phases have been shown to have partial substitution of BH_4^- by Cl^- (37% and 15% substitution, respectively). However, it is not clear if Cl^- substitution is a prerequisite for their stabilities. All of the $Yb(BH_4)_2$ polymorphs (with and without chlorine substitution) have Yb^{2+} octahedrally coordinated by six BH_4^- units.

3.2. Halide-Containing RE-Borohydrides

The large *RE* elements La, Ce, Pr, Nd, Sm and Gd form cubic $LiRE(BH_4)_3Cl$ compounds (space group $I\bar{4}3m$), usually by direct reaction between $LiBH_4$ and $RECl_3$. The first reported member of this series, $LiCe(BH_4)_3Cl$, was structurally characterized by combined SR-PXD and PND on a ^{11}B and D substituted sample [36]. Ce^{3+} is octahedrally coordinated by three Cl^- and three BH_4^- anions. The Ce^{3+} and Cl^- form distorted, isolated Ce_4Cl_4 cubes, and with the three BH_4^- anions coordinating each Ce^{3+}, these units form $[Ce_4(BH_4)_{12}Cl_4]^{4-}$ complex anions that are charge compensated by four Li^+ cations (Figure 7). The Li^+ was reported to fully occupy two crystallographic sites; one two-fold position (2*a*) in the center of the Ce_4Cl_4 cube and one six-fold position (6*b*) which is tetrahedrally coordinated four BH_4^- ions from two different $[Ce_4(BH_4)_{12}Cl_4]^{4-}$ units. Occupation of these two sites is the only way to place the required eight charge compensating Li^+ in the unit cell in an ordered way. Disordered models were not considered during structure determination. Neither PXD nor PND are particularly sensitive to Li, but the proposed structure was found to be stable from density functional theory (DFT) calculations [36]. An alternative study of $LiCe(^{11}BD_4)_3Cl$ also employed SR-PXD, PND and DFT, but considered a variety of disordered distributions of Li^+ within the structure. It was found that a 2/3 occupation of a 12-fold site (12*d*) both gave lower energy (DFT) and slightly better agreement with the diffraction data than the previously reported ordered Li-distribution. The fact that $LiCe(BH_4)_3Cl$ exhibits a high Li-ion conductivity (0.1 mS/cm at RT), further supports the model with disordered Li^+.

$LiRE(BH_4)_3Cl$ with *RE* = La, Pr, Nd, Sm and Gd as well as $LiLa(BH_4)_3X$ with *X* = Br and I have been investigated by lab- or SR-PXD confirming the same structure type as $LiCe(BH_4)_3Cl$ for each of the heavy elements [9,19,37]. The Li-ion conductivities have been measured for *RE* = La, Gd and both compounds show higher conductivities (0.2 and 0.4 mS/cm, respectively) than $LiCe(BH_4)_3Cl$ [9]. This indicates that the Li-ions also partially occupy the 12d site in these compounds.

Non-stoichiometric chloride-containing borohydrides, $NaY(BH_4)_{2-x}Cl_{2+x}$, $LiYb(BH_4)_{4-x}Cl_x$ and $Yb(BH_4)_{2-x}Cl_x$, where chloride anions partly substitute BH_4^- have also been reported [29,31,38].

The halide containing compounds are summarized in Table 3.

Table 3. Halide containing rare earth borohydrides.

Cation		Composition	Crystal System	Space Group	Ref.
Li^+	La^{3+}	$LiLa(BH_4)_3Cl$	Cubic	$I\bar{4}3m$	[9,19,37]
Li^+	La^{3+}	$LiLa(BH_4)_3Br$	Cubic	$I\bar{4}3m$	[37]
Li^+	La^{3+}	$LiLa(BH_4)_3I$	Cubic	$I\bar{4}3m$	[37]
Li^+	Ce^{3+}	$LiCe(BH_4)_3Cl$	Cubic	$I\bar{4}3m$	[8,19,36]
Li^+	Pr^{3+}	$LiPr(BH_4)_3Cl$	Cubic	$I\bar{4}3m$	[19]
Li^+	Nd^{3+}	$LiNd(BH_4)_3Cl$	Cubic	$I\bar{4}3m$	[19]
Li^+	Sm^{3+}	$LiSm(BH_4)_3Cl$	Cubic	$I\bar{4}3m$	[19]
Li^+	Gd^{3+}	$LiGd(BH_4)_3Cl$	Cubic	$I\bar{4}3m$	[9]
Na^+	Y^{3+}	$NaY(BH_4)_{2-x}Cl_{2+x}$	Monoclinic	$P2/c$	[31,38]
Li^+	Yb^{3+}	$LiYb(BH_4)_{4-x}Cl_x$	Tetragonal (x ~1.0)	$P\bar{4}2c$	[29]
	Yb^{2+}	$Yb(BH_4)_{2-x}Cl_x$	Orthorhombic (x = 0.3)	$Pbca$	[29]
			Tetragonal (x = 0.76)	$P\bar{4}$	[29]

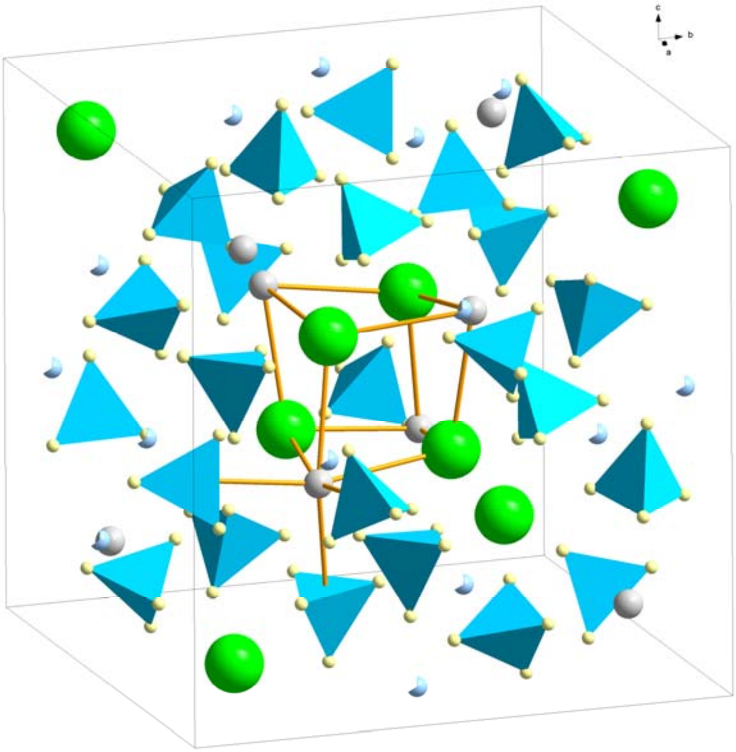

Figure 7. Crystal structure of $LiRE(BH_4)_3Cl$, space group $I\bar{4}3m$. The pseudocube of three Cl^- (green) and three *RE* (white) is outlined as well as the octahedral coordination of RE^{3+} by three Cl^- and three BH_4^- (blue tetrahedra). Li^+ (blue) in partly occupied 12*d* sites are indicated.

3.3. Bi- and Trimetallic RE-Borohydrides

$LiSc(BH_4)_4$ (space group $P\bar{4}2c$) was the first reported bimetallic borohydride [39]. It consists of distorted tetrahedral $[Sc(BH_4)_4]^-$ complex anions with charge compensating Li^+ (Figure 8). The Li^+ atoms have a disorder distributed over half-occupied sites (4*k*) along the tetragonal *c*-axis. The same structure type has also been found for $LiRE(BH_4)_4$ where *RE* = Y [10,40], Yb [29] (with 25% of BH_4^-

substituted by Cl^-) and Lu [19]. The only difference from the $LiSc(BH_4)_4$ structure is that Li^+ were reported in a fully occupied 2-fold site (2*a*), tetrahedrally coordinated by $4BH_4^-$ for *RE* = Y and Yb. This site is situated in the middle of the partly occupied sites in $LiSc(BH_4)_4$. No structure refinement has been performed for $LiLu(BH_4)_4$. Li-ion conductivity has not been measured for $LiSc(BH_4)_3$, but $LiY(BH_4)_4$ shows low conductivity (10^{-6} S/cm at RT).

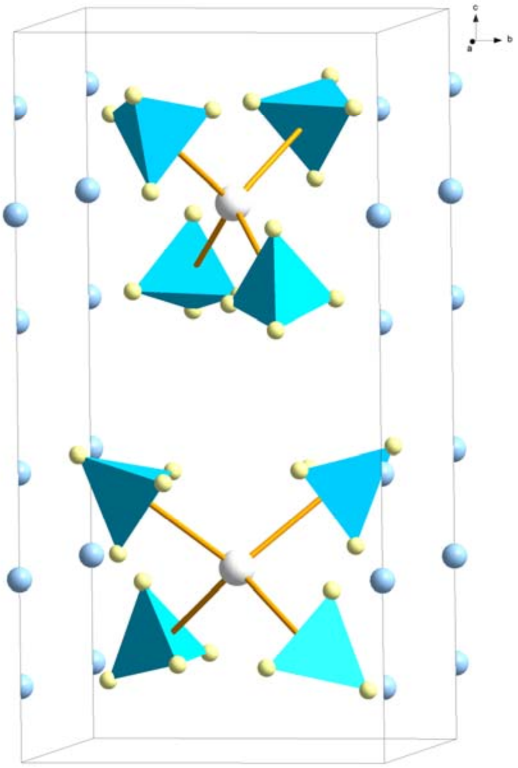

Figure 8. Crystal structure of Li*RE*$(BH_4)_4$, space group $P\bar{4}2c$. The $Sc(BH_4)_4^-$ complex ions are outlined (Sc^{3+}—white, BH_4^-—blue tetrahedra). Both the half-occupied 4k site (*RE* = Sc) and the fully occupied 2*a* site (*RE* = Y, Yb, Lu) for Li^+ (blue) are indicated.

$NaSc(BH_4)_4$ exists in an orthorhombic crystal structure (space group *Cmcm*) which contains tetrahedral $[Sc(BH_4)_4]^-$ complex anions that are less distorted than in $LiSc(BH_4)_4$ [41]. Na^+ has a higher coordination number than Li^+ due to its larger radius, and is octahedrally coordinated by six BH_4^- moieties. The $Na(BH_4)_6$ octahedra form edge-sharing chains along the *c*-axis, with the chains also being interconnected by egde-sharing $Sc(BH_4)_4$ tetrahedra. $NaY(BH_4)_4$ [10,40], $NaEr(BH_4)_4$ [42], $KHo(BH_4)_4$ [32], *o*-$KY(BH_4)_4$ [43], $KEr(BH_4)_4$ [44], and $KYb(BH_4)_4$ [45] are isostructural to $NaSc(BH_4)_4$. $KSc(BH_4)_4$ (space group *Pnma*) contains similar tetrahedral $[Sc(BH_4)_4]^-$ complexes while the coordination number of alkali metal increases further to eight [46].

The BH_4^- anion is isoelectronic with O^{2-} and as such many borohydrides are structurally similar to oxides [33]. The various $Ca(BH_4)_2$ polymorphs are, for instance, similar to TiO_2 polymorphs (Ti^{4+} being isoelectronic to Ca^{2+}) [47]. A series of 20 *RE*-borohydrides with perovskite-like structures have been reported [38,48–53]. Seven of the compounds exhibit face-centered cubic double-perovskite-type structures (space group $Fm\bar{3}$). Despite the high symmetry, the compounds form ordered structures with large unit cell volumes ranging from 1424 Å^3 ($Rb_2LiY(BH_4)_6$) to 1710 Å^3 ($Cs_3Gd(BH_4)_6$). LT-$KYb(BH_4)_3$ (space group $P\bar{4}3m$) exhibits a primitive cubic structure with a much smaller unit cell volume of 176 Å^3 and β-$CsSm(BH_4)_3$ takes the ideal perovskite structure (space group $Pm\bar{3}m$). The rest of the compounds are tetragonal, orthorhombic or monoclinic (Table 4). Using the same analogy to oxide structures, $Li_3K_3La_2(BH_4)_{12}$ and $Li_3K_3Ce_2(BH_4)_{12}$ (space group $Ia\bar{3}d$) are reported to have a garnet-type structure [48].

All other reported bi- and tri-metallic borohydrides with structure types not discussed above, are included in Table 4.

Table 4. Bi- and tri-metallic rare earth borohydrides.

Cations			Polymorph	wt % H	Crystal System	Space Group	Structure Type	Ref.
Li^+	Sc^{3+}		$LiSc(BH_4)_4$	14.5	Tetragonal	$P\bar{4}2c$	New	[39]
Li^+	Y^{3+}		$LiY(BH_4)_4$	10.4	Tetragonal	$P\bar{4}2c$	$LiSc(BH_4)_4$	[10,40]
Li^+	Yb^{3+}		$LiYb(BH_4)_4$	6.7	Tetragonal	$P\bar{4}2c$	$LiSc(BH_4)_4$	[29]
Li^+	Lu^{3+}		$LiLu(BH_4)_4$	6.7	Tetragonal	$P\bar{4}2c$	$LiSc(BH_4)_4$	[19]
Na^+	Sc^{3+}		$NaSc(BH_4)_4$	12.7	Orthorhombic	$Cmcm$	$HT\text{-}CrVO_4$	[41]
Na^+	Y^{3+}		$NaY(BH_4)_4$	9.4	Orthorhombic	Cmcm	$NaSc(BH_4)_4$	[10,40]
Na^+	La^{3+}		$NaLa(BH_4)_4$	7.3	Orthorhombic	$Pbcn$	New	[49]
Na^+	Ce^{3+}		$NaCe(BH_4)_4$	7.3	Orthorhombic	$Pbcn$	$NaLa(BH_4)_4$	[42]
Na^+	Pr^{3+}		$NaPr(BH_4)_4$	7.2	Orthorhombic	$Pbcn$	$NaLa(BH_4)_4$	[42]
Na^+	Er^{3+}		$NaEr(BH_4)_4$	6.5	Orthorhombic	$Cmcm$	$NaSc(BH_4)_4$	[42]
Na^+	Yb^{3+}		$NaYb(BH_4)_4$	6.3	Orthorhombic	$Cmcm$	$NaSc(BH_4)_4$	[45]
K^+	Sc^{3+}		$KSc(BH_4)_4$	11.3	Orthorhombic	$Pnma$	$BaSO_4$	[46]
K^+	Y^{3+}		$o\text{-}KY(BH_4)_4$	8.6	Orthorhombic	$Cmcm$	$NaSc(BH_4)_4$	[38,43]
			$m\text{-}KY(BH_4)_4$		Monoclinic	$C2/c$	$rt\text{-}LaNbO_4$	[38]
K^+	La^{3+}		$K_3La(BH_4)_6$	7.0	Monoclinic	$P2_1/n$	Double-perovskite	[49]
K^+	Ce^{3+}		$K_3Ce(BH_4)_6$	7.0	Monoclinic	$P2_1/c$	Double-perovskite	[48]
K^+	Sm^{2+}		$KSm(BH_4)_3$	5.2	Monoclinic	$P2_1cn$	Perovskite-related	[51]
K^+	Gd^{3+}		$KGd(BH_4)_4$	6.3	Monoclinic	$P2_1/c$	$LiMnF_4$	[52]
			$K_2Gd(BH_4)_5$	6.5	Monoclinic	$P2_1/m$	New	[52]
			$K_3Gd(BH_4)_6$	6.7	Monoclinic	$P2_1/c$	Double-perovskite	[52]
K^+	Ho^{3+}		$KHo(BH_4)_4$	6.1	Orthorhombic	$Cmcm$	$NaSc(BH_4)_4$	[32]
K^+	Er^{3+}		$KEr(BH_4)_4$	6.1	Orthorhombic	$Cmcm$	$NaSc(BH_4)_4$	[44]
K^+	Yb^{2+}		$LT\text{-}KYb(BH_4)_3$	4.7	Cubic	$P\bar{4}3m$	Perovskite-related	[53]
			$HT\text{-}KYb(BH_4)_3$		Orthorhombic	$Pmc2_1$	Perovskite-related	[53]
K^+	Yb^{3+}		$KYb(BH_4)_4$	5.9	Orthorhombic	$Cmcm$	$NaSc(BH_4)_4$	[45]
Rb^+	Y^{3+}		$o\text{-}RbY(BH_4)_4$	6.9	Orthorhombic	$Pnma$	$KSc(BH_4)_4$	[38]
			$m\text{-}RbY(BH_4)_4$	6.9	Monoclinic	$P2_1/c$	Distorted $KSc(BH_4)_4$	[50]
			$Rb_3Y(BH_4)_6$	5.6	Cubic	$Fm\bar{3}$	Double-perovskite	[38,53]
Rb^+	Ce^{3+}		$Rb_3Ce(BH_4)_6$	5.0	Monoclinic	$P2_1/c$	Double-perovskite	[53]
Rb^+	Sm^{2+}		$RbSm(BH_4)_3$	4.3	Orthorhombic	$Pbn2_1$	Perovskite-related	[51]
Rb^+	Eu^{2+}		$RbEu(BH_4)_3$	4.3	Orthorhombic	$Pna2_1$	Perovskite-related	[53]
Cs^+	Y^{3+}		$CsY(BH_4)_4$	5.7	Tetragonal	$I4_1/a$	$CaWO_4$	[50]
			$Cs_2Y(BH_4)_5$	4.2	Hexagonal	$P6_3cm$	new	[38]
			$Cs_3Y(BH_4)_6$		Cubic	$Fm\bar{3}$	Double-perovskite	[38,53]
Cs^+	Sm^{2+}		$\alpha\text{ -}CsSm(BH_4)_3$	3.7	Orthorhomic	$P2_12_12$	Perovskite-related	[51]
			$\alpha'\text{-}CsSm(BH_4)_3$		Tetragonal	$P\bar{4}m2$	Perovskite-related	[51]
			$\beta\text{-}CsSm(BH_4)_3$		Cubic	$Pm\bar{3}m$	Ideal perovskite	[51]
Cs^+	Eu^{2+}		$CsEu(BH_4)_3$	3.7	Tetragonal	$P4/mbm$	Perovskite-related	[53]
Cs^+	Gd^{3+}		$Cs_3Gd(BH_4)_6$	3.8	Cubic	$Fm\bar{3}$	Double-perovskite	[53]
Li^+	K^+	La^{3+}	$Li_3K_3La_2(BH_4)_{12}$	8.1	Cubic	$Ia\bar{3}d$	Garnet	[48]
Li^+	K^+	Ce^{3+}	$Li_3K_3Ce_2(BH_4)_{12}$	8.1	Cubic	$Ia\bar{3}d$	Garnet	[48]
Li^+	Rb^+	Y^{3+}	$Rb_2LiY(BH_4)_6$	6.8	Cubic	$Fm\bar{3}$	Double-perovskite	[38,50]
Li^+	Cs^+	Y^{3+}	$Cs_2LiY(BH_4)_6$	5.4	Cubic	$Fm\bar{3}$	Double-perovskite	[38,50]
Li^+	Cs^+	Ce^{3+}	$Cs_2LiCe(BH_4)_6$	4.8	Cubic	$Fm\bar{3}$	Double-perovskite	[53]
Li^+	Cs^+	Gd^{3+}	$Cs_2LiGd(BH_4)_6$	4.7	Cubic	$Fm\bar{3}$	Double-perovskite	[53]

4. Thermal Properties of Rare Earth Borohydrides

4.1. Monometallic and Halide Substituted Rare Earth Borohydrides

The metathesis reaction between stoichiometric quantities of lithium borohydride $LiBH_4$ and a trivalent rare earth chloride $RECl_3$ results in principle in the formation of either a monometallic trivalent *RE*-borohydride, $RE(BH_4)_3$, $LiRE(BH_4)_4$ or a chloride substituted compound, $LiRE(BH_4)_3Cl$, according to Equations (2)–(4) (see above). During the past seven years extensive efforts have been made to understand the thermal decomposition and rehydrogenation behavior of these compounds.

The following sections summarize the thermal behavior of two compounds: $Y(BH_4)_3$ and $LiCe(BH_4)_3Cl$, which are representative of the monometallic and halide substituted rare earth borohydrides adopting the same structure type.

4.1.1. Yttrium borohydride

$Y(BH_4)_3$ has a high gravimetric hydrogen capacity of 9.1 wt %, and has therefore received considerable interest since 2008 as a potential hydrogen storage material [18]. The stability of crystalline $Y(BH_4)_3$ has been assessed by density functional theory (DFT), and calculations predict the decomposition into boron, yttrium hydride and hydrogen at elevated temperatures. Dai et al. [54] have recently employed first principles calculations to predict the influence of additional alloying elements such as Li, Na, K, Ti, Mn and Ni on the stability and dehydrogenation properties of $Y(BH_4)_3$. The authors concluded that all alloyed systems show smaller enthalpy of decomposition than pure $Y(BH_4)_3$ and that the alkali metals (especially K) may be suitable for improving the dehydrogenation properties of $Y(BH_4)_3$.

Experimental studies regarding the thermal properties of $Y(BH_4)_3$ prepared by liquid phase and mechanochemical synthesis have been described in references [21–23]. According to these reports, α-$Y(BH_4)_3$, which is the stable modification at RT, undergoes a structural transition from the distorted ReO_3-type structure (cubic, $Pa\overline{3}$) into the ordered ReO_3-type structure (cubic, $Fm\overline{3}c$) upon heating to 157–182 °C. In situ SR-PXD measurements on a $LiBH_4$-$Y(BH_4)_3$ (3:1) sample heated under dynamic vacuum with a rate of 2 °C/min up to 450 °C shows the presence of three distinct temperature regions (Figure 9a,b) [21].

LiCl and α-$Y(BH_4)_3$ are the only crystalline phases present in region (I) which spans from RT to 200 °C. The peaks originating from $Y(BH_4)_3$ begin to decrease in intensity at 182 °C and completely disappear at 200 °C. The formation of β-$Y(BH_4)_3$ was not observed under the current experimental conditions, which suggests that the heating rate of 2 °C/min is probably too fast compared to the kinetics of the phase transformation. In region (III), above 262 °C, the pattern shows that LiCl and YH_3 were the only crystalline materials present. In region (II), between 200 and 247 °C, the major crystalline phases are LiCl and YH_3. Additionally, weaker peaks of a new phase emerge at around 200 °C gain in intensity up to 232 °C and diminish again until they finally disappear above 247 °C. Peak indexing and unit cell determination for this intermediate phase have indicated that it might be described in a primitive orthorhombic unit cell with lattice parameters a = 12.170(14) Å, b = 7.670(5) Å, and c = 7.478(6) Å. Similarly, Ravnsbæk et al. [22] have observed the formation of two unidentified compounds after the decomposition of $Y(BH_4)_3$ in the temperature range ~190 to 235 °C. The authors suggested that one of the phases has a composition similar to $Y(BH_4)Cl_2$ or $Y(BH_4)_2Cl$, while the other phase could be a decomposition product containing Y-B-Cl. Jaroń and Grochala [20] attempted to follow the thermal decomposition of $Y(BH_4)_3$ by heating samples in alumina crucibles inside a TG-DSC (Thermogravimetric-differential calorimeter) up to selected temperatures of 194, 210 and 229 °C followed by rapid cooling. The PXD patterns above 229 °C only show the presence of LiCl, with other decomposition products being amorphous. The partially decomposed samples possess a layered morphology and progressive color changes from white to light yellow, brown and finally black at high temperatures. This color change is attributed to the presence of amorphous decomposition products such as polymeric $(B_xH_y)_n$ compounds as well as H-poor Y-B-H phases. The same authors also studied the hydrogen desorption kinetics of α-$Y(BH_4)_3$ as well as that of the HT modification of β-$Y(BH_4)_3$. They observed significant differences below 260 °C for both phases, the decomposition being faster and more facile for the HT phase which they attributed to a three times lower activation energy for thermal decomposition as compared to the low-temperature polymorph [24]. Remhof et al. studied the thermal decomposition of pure $Y(BH_4)_3$ prepared by direct, solvent-free synthesis from YH_3/YH_2, B_2H_6 and H_2 via reactive milling [55]. They observed the onset for hydrogen desorption at 187 °C and a maximum desorption rate of 0.12 wt % H_2/min at 250 °C when the materials were heated with 1 °C/min under 1 bar H_2. Time-resolved in situ PXD data with a low heating rate of 0.2 °C/min collected between RT and 450 °C under 1 bar of hydrogen showed only reflections from $Y(BH_4)_3$ and unreacted YH_3 up to 207 °C, while at 247 °C the Bragg peaks originating from $Y(BH_4)_3$ disappeared and only YH_3 remained visible. No structural transition from the α- to the β-phase was observed. Above 347 °C the decomposition was completed and no further change in the peak intensities was observed until the transformation of YH_3 into YH_2 proceeded at 447 °C. The authors also reported the appearance of at least one amorphous phase in addition to YH_3. However, they did not provide any insight as to the nature of these additional phases. Finally, Park et al. have undertaken a comparative study between $Y(BH_4)_3$ synthesized from $LiBH_4$-YCl_3 (3:1 and 4:1 ratios) by mechanochemistry and via direct synthesis from YH_3, B_2H_6 and H_2 [56]. The authors arrived at the conclusion that both methods result in products that possess distinctly different polymorphic phase transformation, melting behavior and even altered decomposition pathways. In fact, it turned out that the side product LiCl in the metathesis reaction cannot be regarded as inert as it shifts the melting temperature of $Y(BH_4)_3$ and apparently promotes the formation of YB_4 during decomposition which is otherwise absent in the case of $Y(BH_4)_3$ obtained from gas-solid reaction between YH_3, B_2H_6 and H_2.

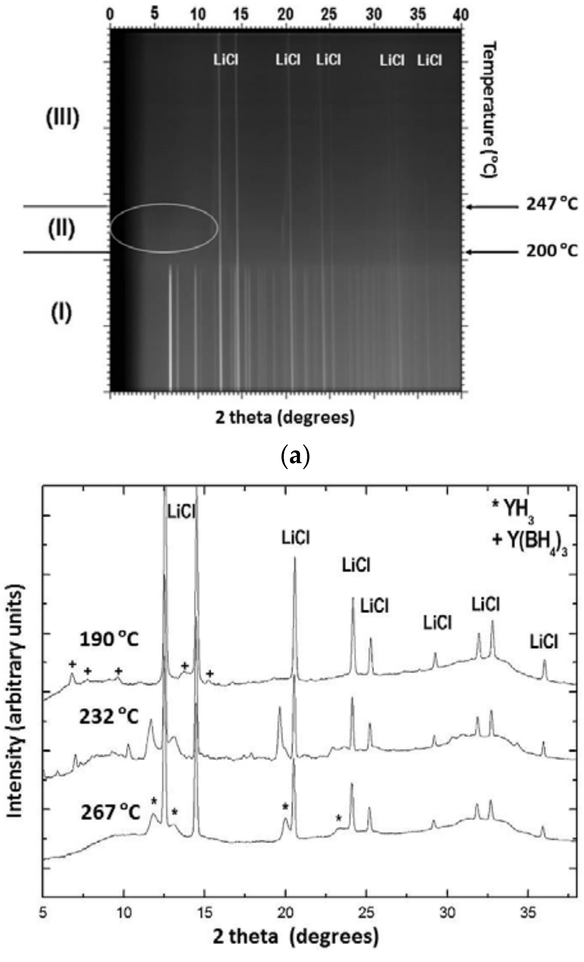

(**a**)

(**b**)

Figure 9. (**a**) SR-PXD pattern of $Y(BH_4)_3$ in the temperature range of 22–450 °C. The sample was heated under dynamic vacuum with a heating rate of 2 °C/min. Three distinct regions have been highlighted and the temperature region for the appearance of an intermediate phase has been encircled; (**b**) Representative SR-PXD patterns at selected temperatures: the top pattern at 190 °C shows remanence of the low-temperature LT phase of $Y(BH_4)_3$, the bottom pattern at 267 °C shows YH_3, and the middle pattern (232 °C) exhibits YH_3 and an additional intermediate phase.

4.1.2. Lithium Cerium Borohydride Chloride

$LiCe(BH_4)_3Cl$ can be obtained via mechanochemical synthesis between three molar equivalents of $LiBH_4$ and one molar equivalent of $CeCl_3$ [8,36]. The thermal decomposition of $LiCe(BH_4)_3Cl$ has been studied in reference [36] by a combination of TG-DSC and residual gas analysis (RGA) with a low heating rate of 2 °C/min under argon flow. According to this report, decomposition proceeds in a two-step process with minor gas release at about 215 °C followed by the major decomposition step at a peak temperature of 246 °C. RGA shows a more than 100 times higher partial pressure for hydrogen than for B_2H_6 and its fragments B_2H_5, B_2H_4 and BH_3. This indicates that the decomposition proceeds almost exclusively by release of hydrogen and that boron is thus kept in the solid state, which is one of the prerequisites for reversible hydrogen storage in borohydrides. Ley et al. [8] have performed Sieverts measurements on a sample containing only $LiCe(BH_4)_3Cl$ and LiCl which show a gas release of 3.75 wt % H_2 during the first desorption and 1.25 wt % H_2 during the second and third desorption. Samples containing one equivalent excess of $LiBH_4$ show a different thermal behavior and exhibit a gas release of 0.5 wt % H_2 up to 220 °C, while 3.25 wt % H_2 are released between 220 and 270 °C. An additional amount of 0.8 wt % H_2 is released between 270 and 500 °C, while during a subsequent isotherm (3 h) about 0.15 wt % H_2 are released. Thus a total amount of 4.7 wt % H_2 are desorbed during heating to 500 °C, while after rehydrogenation at 400 °C and 100 bar for 24 h, about 1.8 wt % of H_2 are desorbed during the second dehydrogenation [8].

In situ SR-PXD experiments have been conducted on the hydride and deuteride form of $LiCe(BH_4)_3Cl$ in order to determine the decomposition products and formation of possible intermediates [8,36]. Figure 10a shows the evolution of powder patterns between 80 and 600 °C with a heating rate of 2 °C/min for a ($3LiBD_4$-$CeCl_3$) mixture obtained after ball milling. Figure 10b displays powder patterns at selected temperatures in more detail.

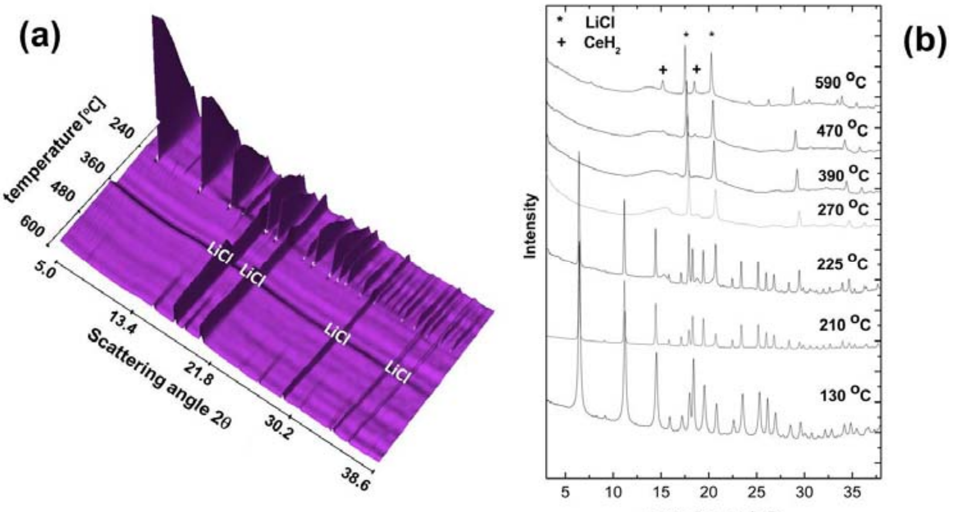

Figure 10. (**a**) In situ SR-PXD data between 80 and 600 °C for a ($3LiBD_4$-$CeCl_3$) mixture after ball milling (6 h); (**b**) Selected powder patterns between 130 and 590 °C. The heating rate was 2 °C/min. Peak positions of major phases are indicated in the plots.

The only crystalline phases present after ball milling are $LiCe(BD_4)_3Cl$ and LiCl. In the low-temperature region between 80 and 150 °C, the crystallinity of the material increases upon heating. As a result the X-ray profiles become narrower and the overall peak intensity increases. Peak intensities for $LiCe(BD_4)_3Cl$ decrease rapidly above 230 °C up to its decomposition peak temperature of 240 °C. Between 270 and 450 °C the SR-PXD pattern exhibits peaks belonging to LiCl only, and a modulated background with a broad and featureless region around 2θ = 10–15°, which is characteristic of some amorphous boron-containing compounds such as Ce-B-D or B-D species. Above 450 °C, new peaks emerge and gain intensity up to the maximum temperature of 600 °C. They can be assigned to CeD_2, and have been highlighted in Figure 10b. The formation of cerium borides such as CeB_4 or CeB_6 could not be observed under the applied experimental conditions. Ley et al. performed in situ SR-PXD studies with a high heating rate of 8 °C/min up to 500 °C on several $n$$LiBH_4$-$CeCl_3$ mixtures (n = 3, 4) [8]. The authors observe the decomposition of $LiCe(BH_4)_3Cl$ at 240 °C similar to [36], and the appearance of an unknown phase above 240 °C—possibly a ternary salt composed of lithium cerium and chloride. Major decomposition products at 500 °C are CeH_2 and CeB_6. Crystalline CeB_6 has also been obtained by Liu et al. [26] while heating up a $3LiBH_4$-$CeCl_3$ mixture to 600 °C for an extended period of time. None of the studies found any indication that favored the formation of boron over CeB_6. Based on those findings the thermal decomposition of $LiCe(BH_4)_3Cl$ is therefore believed to proceed via Equation (5) rather than via Equation (6):

$$LiCe(BH_4)_3Cl \rightarrow \frac{1}{2}CeH_2 + \frac{1}{2}CeB_6 + 11/2H_2 + LiCl \tag{5}$$

$$LiCe(BH_4)_3Cl \rightarrow CeH_2 + 3B + 5H_2 + LiCl \tag{6}$$

The first reaction pathway is furthermore supported by TG-DSC experiments which show a weight loss of 3.5 wt % H_2 for a $3LiBH_4$-$CeCl_3$ hydride mixture after ball milling. This value is in excellent agreement with the expected weight loss of 3.6 wt % H_2, assuming the formation of CeH_2 and CeB_6 in Equation (5).

Trends in the thermal decomposition of the monometallic and halide substituted *RE*-borohydrides are difficult to establish despite an increasing number of publications in the field. This complication is mainly due to the use of different preparation methods e.g., mechanochemistry vs. wet-chemistry. Ball milling of $LiBH_4$-$RECl_3$ mixtures always yields LiCl in addition to the *RE*-borohydride which cannot be simply regarded as "dead weight". In fact, its presence can affect the melting point, phase transformation temperatures, induce halide substitution and even alter the decomposition pathway. Wet-chemical methods have therefore been developed which can separate the alkali metal chloride from the metal borohydride, e.g., through dissolution and/or filtering. However, they lead to the formation of solvated *RE*-borohydrides which have to be carefully dried at elevated temperatures and in vacuo. Here arises another risk in which the solvent cannot be fully removed or that the metal borohydride partially decomposes during the drying process. A second factor is based on the use of different characterization methods such as calorimetry and in situ powder diffraction in which vastly different experimental conditions are employed. In the case of calorimetric studies the purge gas (Ar/He/H_2), heating rate, sample mass and choice of sample container (Al/Al_2O_3) have a profound effect on the number, intensity, shape and position of the registered heat flow signals. In the case of in situ diffraction the use of H_2-backpresure vs. vacuum is known to alter the decomposition pathway. Furthermore, reactions between the borohydrides and the sample holder (mainly sapphire) at high temperature in connection with micro-leaks have led to the formation of oxide species on several occasions [57].

A correlation between the decomposition temperature of the metal borohydrides and their Pauling electronegativity was already suggested in 1955 [58,59] and has been thoroughly investigated by several research groups both experimentally and theoretically [12]. The more stable alkali metal borohydrides tend to show a linear correlation between the decomposition temperature and the electronegativity of the metal cation.

However, compounds formed by metals with higher electronegativity tend to deviate from this linear behavior. An exponential correlation between the decomposition temperature and the electronegativity of the metal has therefore been suggested instead. Tables 5 and 6 summarize the thermal properties of selected monometallic rare earth borohydrides $RE(BH_4)_n$ (n = 2, 3) and lithium rare earth borohydride chlorides $LiRE(BH_4)_3Cl$.

Table 5. Thermal properties of selected monometallic RE-borohydrides with trivalent cation.

Cation	**Compound**	**T$_{dec}$. (°C)**	**Decompositon Products**	**Comments**	**Ref.**
La^{3+}	$La(BH_4)_3$	258	Not specified	Material obtained from thermolysis of $La(BH_4)_3$ $nS(CH_3)_2$; 8% mass loss due to simultaneous release of B_2H_6 and H_2	[34]
Ce^{3+}	$Ce(BH_4)_3$	251	Not specified	Material obtained from thermolysis of $Ce(BH_4)_3$ $nS(CH_3)_2$; 8.5% mass loss due to simultaneous release of B_2H_6 and H_2	[34]
Pr^{3+}	$Pr(BH_4)_3$	275	No crystalline products	Sample synthesized in toluene and DMS. In situ SR-PXD showed no crystalline decomposition product until 500 °C.	[30]
Gd^{3+}	$Gd(BH_4)_3$	260	Not specified	Sample obtained from thermal decomposition of $Gd(BH_4)_3$*$nS(CH_3)_2$; DSC shows endothermic event at 260 °C related to hydrogen desorption. MS shows minor contributions of B_2H_6 between 225 and 275 °C.	[60]
Tb^{3+}	$Tb(BH_4)_3$	213 and 253	Not specified	$3LiBH_4$-$TbCl_3$ mixture after ball milling (2 h). DSC trace shows two endothermic events with peak temperatures of 213 and 253 °C	[19]
Dy^{3+}	$Dy(BH_4)_3$	No data	No data	Only structural information available; decomposition is believed to occur similar to $Y(BH_4)_3$ and $Gd(BH_4)_3$	[18]
Ho^{3+}	$Ho(BH_4)_3$	170 225 255	No crystalline products	Three distinct endothermic events visible in the DSC up to 400 °C; onset of hydrogen release observed at 170 °C with the fastest rate at 255 °C	[32]
Er^{3+}	$Er(BH_4)_3$	230	ErH_2 and ErB_4	Hydrogen desorption starts at 230 °C; multiple endothermic events visible in DSC; 3.2% mass loss observed up to 400 °C	[30]

Table 6. Thermal properties of lithium rare earth borohydride chlorides.

Cation1	**Cation 2**	**Compound**	**T$_{dec.}$ (°C)**	**Decompositon Products**	**Comments**	**Ref**
La^{3+}	Li^{+}	$LiLa(BH_4)_3Cl$	226 and 266	LaH_2 and LaB_6	TG/DSC shows two endothermic events between 200 and 300 °C and total mass loss of 2.87%	[9]
Ce^{3+}	Li^{+}	$LiCe(BH_4)_3Cl$	[a] 215, [a] 246, [b] 240, [b] 266	CeH_2 and CeB_6	[a] $3LiBD_4$-$CeCl_3$ mixture after ball milling; two endothermic events at 215 and 246 °C observed by DSC [b] $3LiBH_4$-$CeCl_3$ mixture after ball milling: major DSC events at 213 (melting), 240, and 266 °C (both decomposition)	[8,36]
Pr^{3+}	Li^{+}	$LiPr(BH_4)_3Cl$	[a] 176 [b] 212 and 247	PrH_3 and PrB_6	[a] Synthesised in $(C_2H_5)_2O$. Sample is a mixture between $Pr(BH_4)_3$ and $LiPr(BH_4)_3Cl$; T$_{dec}$ determined by TG/DSC [b] $3LiBH_4$-$PrCl_3$ mixture after ball milling.TG/DSC shows two endothermic events at 212 °C and 247 °C with 0.7% and 2.6% mass loss, respectively	[30]
Nd^{3+}	Li^{+}	$LiNd(BH_4)_3Cl$	223 and 241	Not specified	$3LiBH_4$-$NdCl_3$ mixture after ball milling. TG/DSC shows two endothermic events at 223 °C and 241 °C with 0.4% and 2.4% mass loss respectively	[19]
Gd^{3+}	Li^{+}	$LiGd(BH_4)_3Cl$	261	GdB_4	Value determined from thermogravimetric experiment	[9]

For the monometallic trivalent compounds the decomposition temperature decreases with increasing electronegativity of the metal. It reaches its highest value of 258 °C for $La(BH_4)_3$, 275 °C for $Pr(BH_4)_3$, and 260 °C for $Gd(BH_4)_3$ [30,34,60], and drops to 230 °C in the case of $Er(BH_4)_3$ [30]. Ultimately the decomposition reaction results in the formation of the corresponding rare earth hydrides and borides which is favored over the formation of elemental boron for technological applications. Crystalline decomposition products are not always formed, however, even when heating the materials to 400–500 °C, as is the case for $Pr(BH_4)_3$ and $Ho(BH_4)_3$ [30,32]. The thermal decomposition of the Li*RE*$(BH_4)_3$Cl-type compounds appears to be more complex and proceeds via a multi-step process involving at least two different steps over a temperature range of up to 50 °C. The highest decomposition temperature of 266 °C is observed for $LiLa(BH_4)_3Cl$ while $LiNd(BH_4)_3Cl$ possesses the lowest one with 241 °C. The variation in decomposition temperature is far less pronounced in the rare earth borohydrides as compared to alkali or alkaline earth borohydrides though. This is not unexpected since the range of electronegativity observed for the lanthanides is rather small and increases only moderately from 1.10 for Lanthanum to 1.23 for Erbium. In case of the $Li\mathit{RE}(BH_4)_3Cl$-type compounds the less electronegative alkali metal (Li) shows dominantly ionic interactions and the overall stability of compound is controlled by the more electronegative cation (*RE*) which is in fact part of a complex anion $[\mathit{RE}_4Cl_4(BH_4)_{12}]^{4-}$. The difference of 25 °C in decomposition temperatures between $LiLa(BH_4)_3Cl$ and $LiNd(BH_4)_3Cl$ indicates that the decomposition temperatures are specific for these complex anions and directly reflects differences in their stability [1].

4.2. Composites Containing *RE*-Borohydrides and $LiBH_4$

$LiBH_4$ has the highest theoretical hydrogen storage capacity (18.5 wt % H_2) of all borohydrides of which 13.9 wt % H_2 are accessible through Equation (7):

$$LiBH_4 \rightarrow LiH + B + 3/2H_2 \quad (7)$$

However, harsh pressure and temperature conditions are necessary to reversibly release (>400 °C) and reabsorb (150 bar H_2; 650 °C) hydrogen from $LiBH_4$ due to its high thermal stability ($\Delta H = 74$ kJ/mol H_2) [61]. The *RE*-borohydrides on the other hand decompose between 200 and 300 °C, which is significantly lower than the decomposition temperature of $LiBH_4$. There has been considerable interest in utilizing *RE*-borohydrides as part of a composite mixture with other light weight metal borohydrides such as $LiBH_4$. The general idea behind the use of composite mixtures over pure compounds is to reduce the enthalpy and consequently the hydrogen desorption temperature of the more stable $LiBH_4$. Indeed, additives such as MgH_2 [62,63], CaH_2 [64,65], CeH_2/LaH_2 [66] and Al [67,68] have been used successfully to lower the stability of $LiBH_4$ by the formation of MgB_2, CaB_6 and AlB_2, respectively. For a composite containing $LiBH_4$-MgH_2 (2:1), a two-step decomposition is observed at high temperatures (>400 °C) [62,63,69] while for $LiBH_4$-CaH_2 (6:1) decomposition occurs in a single step reaction, which is advantageous for reversible hydrogen storage applications [64]. In addition to hydrides, halides such as $TiCl_3$, TiF_3 and ZnF_2 have been recently employed to reduce the decomposition temperature of $LiBH_4$ through cation exchange and formation of an unstable transition metal borohydrides [70]. $LiBH_4$ has also been destabilized by the addition of $FeCl_2$, $CoCl_2$ and $NiCl_2$, however, in the case of $CoCl_2$, diborane is released during dehydrogenation which results in capacity loss [71]. Gennari et al. showed that composites of $6LiBH_4 + \mathit{RE}Cl_3$ (*RE* = Ce, Gd) form *RE*-hydrides during thermal decomposition which in turn destabilize the remaining $LiBH_4$ [28]. A composite mixture of $LiBH_4$-$CeCl_3$ (6:1) showed a reversible capacity of 40% after rehydrogenation at 60 bar and 400 °C. In addition, a change in the decomposition pathway and increased formation of CeB_6 and GdB_4 has been reported for composites desorbed against 5 bar of hydrogen pressure as compared to vacuum [28]. In order to promote the reversibility of CeB_6 formed during the decomposition of $Ce(BH_4)_3$, the same authors added LiH to as-milled $LiBH_4$-$CeCl_3$ (6:1) composites and then further milled for 1 h. PXD data showed the presence of LiCl and CeH_{2+x} after the final milling step. Such a $LiBH_4$-$CeCl_3$-LiH (6:1:3) composite released 5.3 wt % H_2 during the first dehydrogenation and 4.4 wt % H_2 during the second cycle after rehydrogenation under relatively mild conditions (400 °C, 60 bar, 2 h) which corresponds to 80% reversible capacity.

Olsen et al. have intensively studied the structure, thermal behavior and hydrogen storage properties of a series of $LiBH_4$-$\mathit{RE}Cl_3$ (*RE* = La, Ce, Pr, Nd, Sm, Eu, Gd, Tb, Er, Yb and Lu) composites obtained by ball milling $LiBH_4$ and the respective *RE*-chlorides in a molar ratio of 6:1 [19]. The systematic study has shown that ball milling results in the formation of either $Li\mathit{RE}(BH_4)_3Cl$ (*RE* = La, Ce, Pr, Nd, Sm, Gd), α,β-$\mathit{RE}(BH_4)_3$ (*RE* = Sm, Gd, Tb, Dy, Er Tm and Yb) or Li*RE*(BH_4)$_4$ (*RE* = Yb, Lu) together with excess $LiBH_4$ [19]. TG-DSC combined with in/ex situ PXD show that the composites which contain Li*RE*(BH_4)$_3$Cl decompose at around 200 °C, and exhibit multiple decomposition steps with the formation of several intermediate phases. The remaining $LiBH_4$ in these composites decomposes and releases hydrogen below 350 °C, which is much lower than the decomposition temperature of pure $LiBH_4$ [61]. In contrast, the thermal decomposition of the composites which contain α,β-*RE*(BH_4)$_3$ and excess $LiBH_4$, proceeds with only two major decomposition steps in the temperature range 250–350 °C. Common to all composites, is the formation of *RE*H_2 as the main decomposition product and *RE*B_n (n = 4, 6) species at temperatures in excess of 400 °C. It was concluded that the presence of *RE*H_2 has a destabilizing effect on the remaining $LiBH_4$ in all the composites, as was already exemplary reported by Gennari et al. for *RE* = Ce and Gd [28]. Rehydrogenation of the La-system under 100 bar and 300 °C showed only very limited rehydrogenation capacity of 18%, whereas rehydrogenation of the Er-system (100 bar, 400 °C) showed a slightly higher capacity of 25% [19].

More recently, a selection of composites containing either La, Er or Pr have been synthesized to determine whether the composites obtained by mechanochemistry differ from those made by wet-chemical methods [30,72,73]; whether the composites which contain alkali chlorides as by-products show a different thermal behavior from those which are halide-free; and determine the role of additives such as LiH for the rehydrogenation behavior of the composites. Composite mixtures of *RE*-borohydrides of La, Er and $LiBH_4$ and LiH were obtained by mechanochemical methods [72]. Ex situ PXD and TG-DSC measurements showed that heating to 400 °C yielded LaB_6, ErB_4 and *RE*$H_{2+\delta}$ ($0 < \delta < 1$) as major decomposition products and that $LiBH_4$ was destabilized by *RE*$H_{2+\delta}$ formed through decomposition of the parent borohydrides $LiLa(BH_4)_3Cl$ and $Er(BH_4)_3$, respectively. Therefore, its decomposition temperature was reduced by as much as 100 °C compared to that of pure ball milled $LiBH_4$. The La-containing composite showed only a limited reversible capacity of 20% (340 °C, 100 bar), probably caused by hydrogen uptake of some amorphous boron-containing phases; similar to the limited rehydrogenation capacity found in the $6LiBH_4$-$LaCl_3$ composite after ball milling that did not contain additional LiH [19]. In contrast, the erbium-containing $6LiBH_4$-$ErCl_3$-$3LiH$ composite showed more promising hydrogen storage properties and could be rehydrogenated at 340 °C and 100 bar hydrogen to a large extent. Such a composite mixture showed a reversible capacity of 66% when desorbed in vacuo, which increased to 80% when desorbed against 5 bar of hydrogen backpressure.

The structure and thermal properties of halide-free *RE*-borohydrides (*RE* = Pr, Er) have also been obtained by solvent-based synthesis instead of mechanochemistry [30,73]. Both compounds showed a simple decomposition pathway into the corresponding hydrides and borides according to Equations (8) and (9):

$$Er(BH_4)_3 \rightarrow 0.75ErB_4 + 0.25ErH_2 + 5.75H_2 \quad (8)$$

$$Pr(BH_4)_3 \rightarrow 0.5PrB_6 + 0.5PrH_2 + 5.5H_2 \quad (9)$$

Rehydrogenation of both materials was monitored by ex situ and in situ SR-PXD measurements at 340 °C and hydrogen pressures of up to 100 bar. However, no new crystalline phases were observed. In addition, TG-DSC experiments of the samples exposed to 100 bar of hydrogen for 21 h showed the absence of any mass loss and heat flow signals, indicating that rehydrogenation was unsuccessful. These findings are in disagreement with Gennari et al. who reported that $Er(BH_4)_3$ synthesized by ball milling had a reversible hydrogen capacity of 20% (rehydrogenation at 400 °C, 60 bar H_2) [74]. This "partial reversibility" for several *RE*-borohydride containing composites of the mechanomilled materials is most likely due to the rehydrogenation of $LiBH_4$ and not due to the formation of the *RE*-borohydrides from the corresponding *RE*-hydrides or borides.

The decomposition and rehydrogenation behavior of composite mixtures containing the halide-free $Er(BH_4)_3$ ball milled for one hour in the presence of $LiBH_4$ and/or LiH has been further investigated in reference [73]. Two composites were studied in detail: $Er(BH_4)_3$-LiH (1:6) and $LiBH_4$-$Er(BH_4)_3$-LiH (3:1:3). Hydrogen sorption measurements in a Sieverts-type apparatus for the 3:1:3 composite showed a hydrogen release of 4.2, 3.7 and 3.5 wt % H_2 during three desorption-absorption cycles (des: 400 °C, 5–10 bar H_2; abs: 340 °C, 100 bar H_2) and thus good rehydrogenation behavior with reversible hydrogenation capacity in the range of 80–85%. This halide-free composite showed similar behavior to a $6LiBH_4$-$ErCl_3$-3LiH composite mixture [72] obtained by ball milling. In both systems, the major decomposition products were $ErH_{2+\delta}$ ($0 < \delta < 1$) and ErB_4 while rehydrogenation leads to the formation of ErH_3 and the rehydrogenation of $LiBH_4$. Between the two studies, minor differences were observed in the number and variety of ErH_3 polymorphs formed upon rehydrogenation. While cubic-ErH_3 was the only polymorph reported in [72], a mixture of tetragonal-ErH_3 and cubic-ErH_3 polymorphs were reported after rehydrogenation (340 °C, 93 bar H_2) in [73].

The influence of additives such as LiH on the rehydrogenation behavior of $Er(BH_4)_3$ was investigated in reference [30]. For this purpose, halide-free $Er(BH_4)_3$ was decomposed at 400 °C and rehydrogenated at 340 °C and 100 bar of hydrogen. PXD experiments on the desorbed and rehydrogenated samples did not show any crystalline phases while TG-DSC data measured for the rehydrogenated sample did not show any mass loss and no heat flow signal up to 400 °C (Figure 11). In two control experiments, either 100 wt % of LiCl or 50 wt % of LiH were added to the halide-free $Er(BH_4)_3$ samples, and decomposed and rehydrogenated as before.

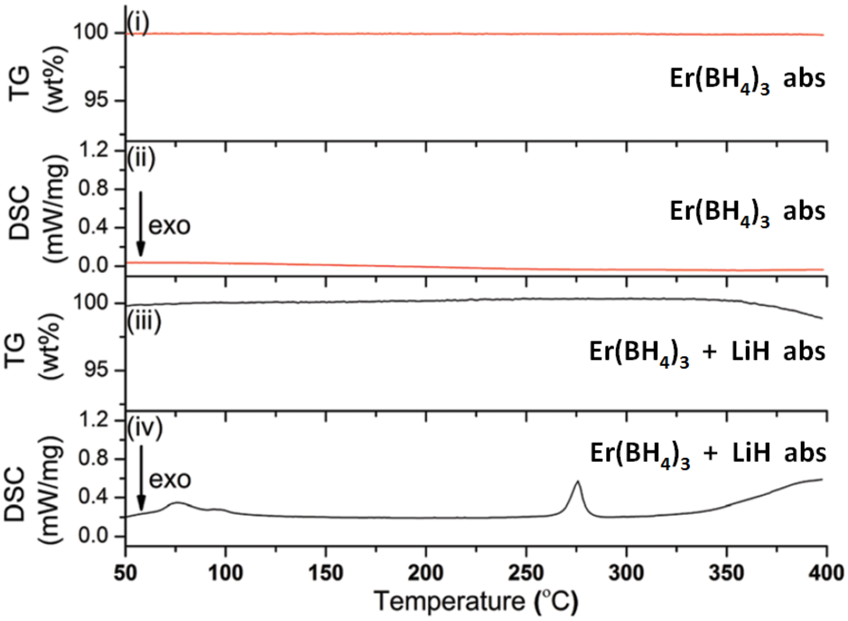

Figure 11. TG data ((**i**) and DSC heat flow signal (**ii**) of halide-free $Er(BH_4)_3$ after one desorption (des)-absorption (abs) cycle; TG-data (**iii**) and DSC heat flow signal (**iv**) of a mixture containing $Er(BH_4)_3$ and 50 wt % LiH after one des-abs cycle (des: 400 °C, 5 bar H_2; abs: 340 °C, 100 bar H_2 for both cases) [30].

The composite mixture containing additional LiCl did not show any crystalline phases after rehydrogenation. Neither heat flow signals nor weight loss could be detected after rehydrogenation which clearly demonstrated that the presence of LiCl had no beneficial effect on the rehydrogenation behavior. The composite mixture containing 50 wt % LiH was studied by in situ SR-PXD (Figure 12). While the ball milled sample mainly showed the presences of LiH and a modulation of the background indicative of some amorphous boron-containing phases such as ErB_4 when heated from RT to 400 °C, the rehydrogenated material (100 bar H_2) showed the evolution of peaks belonging to ErH_3 at 400 °C and upon cooling to RT the appearance of peaks originating from *h*-$LiBH_4$.

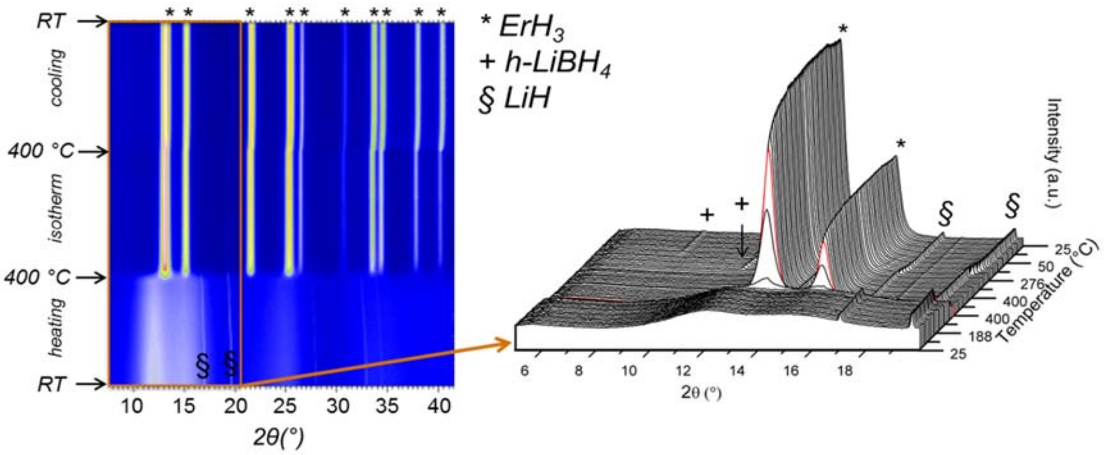

Figure 12. In situ SR-PXD data of a powder mixture containing desorbed $Er(BH_4)_3$ + 50 wt % LiH. The composite was heated from RT to 400 °C followed by a 1 h isotherm and cooled to RT in $p(H_2)$ = 100 bar (temperature ramp of 5 °C/min). The inset illustrates a magnification of the 2θ range from 5 to 20° to enhance the visibility of Bragg peaks for *h*-$LiBH_4$ (+). The red curve in the magnified section is the diffraction pattern measured at 400 °C. λ = 0.69733 Å.

The unsuccessful rehydrogenation of the composites containing LiCl vs. LiH clearly demonstrates that the influence of LiH as an additive goes beyond simply being a source of Li-ions. The successful formation of $LiBH_4$ for the LiH-containing composite is an analogous to that of similar reactive hydride composites with LiH, such as LiH + MgB_2. In the latter case, however, much harsher conditions or the use of additional catalysts is necessary [62,75].

5. Conclusions

The past 10 years have led to the discovery of a multitude of new borohydrides containing *RE* elements which show rich chemistry, structural diversity and a wide range of compositions. Their application ranges from hydrogen and thermal heat storage to solid state electrolytes. Lately, exciting new fluorescent and magnetocaloric properties have been discovered in several *RE*-borohydrides such as $CsEu(BH_4)_3$ and $K_2Gd(BH_4)_5$ [52,53]. In the future, it will hopefully be possible to design new advanced functional materials based on *RE*-borohydrides with desired compositions and new exciting properties that make their entrance into many more applications and research areas. A promising new field could be the use of *RE*-borohydrides as advanced fast neutron shields [76] for compact and portable neutron sources [77]. Such mobile units are in high demand for materials testing and neutron capture therapy, which is a promising approach to cancer therapy where conventional radiation therapies fail.

Acknowledgments: The research leading to these results has received funding from the People Program (Marie Curie Actions) of the European Union's Seventh Framework Program FP7/2007–2013/ under REA grant agreement n_ 607040 (Marie Curie ITN ECOSTORE) and is thankfully acknowledged. The Research Council of Norway is acknowledged for financial support through the FRIENERGI project and the SYNKNØYT program.

Conflicts of Interest: The authors declare no conflict of interest.

References

1. Paskevicius, M.; Jepsen, L.H.; Schouwink, P.; Cerny, R.; Ravnsbæk, D.B.; Filinchuk, Y.; Dornheim, M.; Besenbacherf, F.; Jensen, T.R. Metal borohydrides and derivatives—Synthesis, structure and properties. *Chem. Soc. Rev.* **2017**, *46*, 1565–1634. [CrossRef] [PubMed]
2. Mohtadi, R.; Orimo, S.I. The renaissance of hydrides as energy materials. *Nat. Rev. Mater.* **2017**, *2*, 16091. [CrossRef]

3. Callini, E.; Atakli, Z.O.K.; Hauback, B.C.; Orimo, S.; Jensen, C.; Dornheim, M.; Grant, D.; Cho, Y.W.; Chen, P.; Hjörvarsson, B.; et al. Complex and liquid hydrides for energy storage. *Appl. Phys. A Mater. Sci. Process.* **2016**, *122*, 353.
4. Li, H.W.; Yan, Y.G.; Orimo, S.; Züttel, A.; Jensen, C.M. Recent Progress in Metal Borohydrides for Hydrogen Storage. *Energies* **2011**, *4*, 185–214. [CrossRef]
5. Orimo, S.I.; Nakamori, Y.; Eliseo, J.R.; Züttel, A.; Jensen, C.M. Complex hydrides for hydrogen storage. *Chem. Rev.* **2007**, *107*, 4111–4132. [CrossRef] [PubMed]
6. Sheppard, D.A.; Paskevicius, M.; Humphries, T.D.; Felderhoff, M.; Capurso, G.; von Colbe, J.B.; Dornheim, M.; Klassen, T.; Ward, P.A.; Teprovich, J.A.; et al. Metal hydrides for concentrating solar thermal power energy storage. *Appl. Phys. A Mater. Sci. Process.* **2016**, *122*, 395. [CrossRef]
7. Møller, K.; Sheppard, D.; Ravnsbæk, D.; Buckley, C.; Akiba, E.; Li, H.-W.; Jensen, T. Complex Metal Hydrides for Hydrogen, Thermal and Electrochemical Energy Storage. *Energies* **2017**, *10*, 1645. [CrossRef]
8. Ley, M.B.; Ravnsbæk, D.B.; Filinchuk, Y.; Lee, Y.S.; Janot, R.; Cho, Y.W.; Skibsted, J.; Jensen, T.R. $LiCe(BH_4)_3Cl$, a New Lithium-Ion Conductor and Hydrogen Storage Material with Isolated Tetranuclear Anionic Clusters. *Chem. Mater.* **2012**, *24*, 1654–1663. [CrossRef]
9. Ley, M.B.; Boulineau, S.; Janot, R.; Filinchuk, Y.; Jensen, T.R. New Li Ion Conductors and Solid State Hydrogen Storage Materials: $LiM(BH_4)_3Cl$, M = La, Gd. *J. Phys. Chem. C* **2012**, *116*, 21267–21276. [CrossRef]
10. Roedern, E.; Lee, Y.S.; Ley, M.B.; Park, K.; Cho, Y.W.; Skibsted, J.; Jensen, T.R. Solid state synthesis, structural characterization and ionic conductivity of bimetallic alkali-metal yttrium borohydrides $MY(BH_4)_4$ (M = Li and Na). *J. Mater. Chem. A* **2016**, *4*, 8793–8802. [CrossRef]
11. Skripov, A.V.; Soloninin, A.V.; Ley, M.B.; Jensen, T.R.; Filinchuk, Y. Nuclear Magnetic Resonance Studies of BH_4 Reorientations and Li Diffusion in $LiLa(BH_4)_3Cl$. *J. Phys. Chem. C* **2013**, *117*, 14965–14972. [CrossRef]
12. Nakamori, Y.; Miwa, K.; Ninomiya, A.; Li, H.W.; Ohba, N.; Towata, S.I.; Züttel, A.; Orimo, S.I. Correlation between thermodynamical stabilities of metal borohydrides and cation electronegativites: First-principles calculations and experiments. *Phys. Rev. B* **2006**, *74*, 045126. [CrossRef]
13. Wiberg, E.; Bauer, R. Zur Kenntnis eines Magnesium-Bor-Wasserstoffs $Mg(BH_4)_2$. *Z. Fur Naturforschung Sect. B J. Chem. Sci.* **1950**, *5*, 397–398. [CrossRef]
14. Goerrig, D. Verfahren zur Herstellung von Boranaten. German Patent DBP 1,077,644, 27 December 1958.
15. Chlopek, K.; Frommen, C.; Leon, A.; Zabara, O.; Fichtner, M. Synthesis and properties of magnesium tetrahydroborate, $Mg(BH_4)_2$. *J. Mater. Chem.* **2007**, *17*, 3496–3503. [CrossRef]
16. Koester, R. Neue herstellungsmethoden für metallborhydride. *Angew. Chem.* **1957**, *3*, 94. [CrossRef]
17. Zanella, P.; Crociani, L.; Masciocchi, N.; Giunchi, G. Facile high-yield synthesis of pure, crystalline $Mg(BH_4)_2$. *Inorg. Chem.* **2007**, *46*, 9039–9041. [CrossRef] [PubMed]
18. Sato, T.; Miwa, K.; Nakamori, Y.; Ohoyama, K.; Li, H.W.; Noritake, T.; Aoki, M.; Towata, S.I.; Orimo, S.I. Experimental and computational studies on solvent-free rare-earth metal borohydrides $R(BH_4)_3$ (R = Y, Dy, and Gd). *Phys. Rev. B* **2008**, *77*, 104114. [CrossRef]
19. Olsen, J.E.; Frommen, C.; Jensen, T.R.; Riktor, M.D.; Sørby, M.H.; Hauback, B.C. Structure and thermal properties of composites with RE-borohydrides (RE = La, Ce, Pr, Nd, Sm, Eu, Gd, Tb, Er, Yb or Lu) and $LiBH_4$. *RSC Adv.* **2014**, *4*, 1570–1582. [CrossRef]
20. Jaroń, T.; Grochala, W. $Y(BH_4)_3$-an old-new ternary hydrogen store aka learning from a multitude of failures. *Dalton Trans.* **2010**, *39*, 160–166. [CrossRef] [PubMed]
21. Frommen, C.; Aliouane, N.; Deledda, S.; Fonneløp, J.E.; Grove, H.; Lieutenant, K.; Llamas-Jansa, I.; Sartori, S.; Sørby, M.H.; Hauback, B.C. Crystal structure, polymorphism, and thermal properties of yttrium borohydride $Y(BH_4)_3$. *J. Alloys Compd.* **2010**, *496*, 710–716. [CrossRef]
22. Ravnsbæk, D.B.; Filinchuk, Y.; Cerny, R.; Ley, M.B.; Haase, D.; Jakobsen, H.J.; Skibsted, J.; Jensen, T.R. Thermal Polymorphism and Decomposition of $Y(BH_4)_3$. *Inorg. Chem.* **2010**, *49*, 3801–3809. [CrossRef] [PubMed]
23. Yan, Y.G.; Li, H.W.; Sato, T.; Umeda, N.; Miwa, K.; Towata, S.; Orimo, S. Dehydriding and rehydriding properties of yttrium borohydride $Y(BH_4)_3$ prepared by liquid-phase synthesis. *Int. J. Hydrogen Energy* **2009**, *34*, 5732–5736. [CrossRef]
24. Jaroń, T.; Kozminskia, W.; Grochala, W. Phase transition induced improvement in H_2 desorption kinetics: The case of the high-temperature form of $Y(BH_4)_3$. *Phys. Chem. Chem. Phys.* **2011**, *13*, 8847–8851. [CrossRef] [PubMed]

25. Gennari, F.C.; Esquivel, M.R. Synthesis and dehydriding process of crystalline Ce$(BH_4)_3$. *J. Alloys Compd.* **2009**, *485*, L47–L51. [CrossRef]
26. Zhang, B.J.; Liu, B.H.; Li, Z.P. Destabilization of $LiBH_4$ by (Ce, La)(Cl, F)$_3$ for hydrogen storage. *J. Alloys Compd.* **2011**, *509*, 751–757. [CrossRef]
27. Humphries, T.D.; Ley, M.B.; Frommen, C.; Munroe, K.T.; Jensen, T.R.; Hauback, B.C. Crystal structure and in situ decomposition of $Eu(BH_4)_2$ and $Sm(BH_4)_2$. *J. Mater. Chem. A* **2015**, *3*, 691–698. [CrossRef]
28. Gennari, F.C.; Albanesi, L.F.; Puszkiel, J.A.; Larochette, P.A. Reversible hydrogen storage from $6LiBH_4$-MCl_3 (M = Ce, Gd) composites by in-situ formation of MH_2. *Int. J. Hydrogen Energy* **2011**, *36*, 563–570. [CrossRef]
29. Olsen, J.E.; Frommen, C.; Jensen, T.R.; Riktor, M.D.; Sørby, M.H.; Hauback, B.C. Crystal structures and properties of solvent-free $LiYb(BH_4)_{4-x}Cl_x$, $Yb(BH_4)_3$ and $Yb(BH_4)_{2-x}Cl_x$. *RSC Adv.* **2013**, *3*, 10764–10774. [CrossRef]
30. Heere, M.; GharibDoust, S.H.P.; Frommen, C.; Humphries, T.D.; Ley, M.B.; Sørby, M.H.; Jensen, T.R.; Hauback, B.C. The influence of LiH on the rehydrogenation behavior of halide free rare earth (RE) borohydrides (RE = Pr, Er). *Phys. Chem. Chem. Phys.* **2016**, *18*, 24387–24395. [CrossRef] [PubMed]
31. Ravnsbæk, D.B.; Ley, M.B.; Lee, Y.S.; Hagemann, H.; D'Anna, V.; Cho, Y.W.; Filinchuk, Y.; Jensen, T.R. A mixed-cation mixed-anion borohydride $NaY(BH_4)_2Cl_2$. *Int. J. Hydrogen Energy* **2012**, *37*, 8428–8438. [CrossRef]
32. Wegner, W.; Jaroń, T.; Grochala, W. Polymorphism and hydrogen discharge from holmium borohydride, $Ho(BH_4)_3$, and $KHo(BH_4)_4$. *Int. J. Hydrogen Energy* **2014**, *39*, 20024–20030. [CrossRef]
33. Cerny, R.; Schouwink, P. The crystal chemistry of inorganic metal borohydrides and their relation to metal oxides. *Acta Crystallogr. Sect. B Struct. Sci. Cryst. Eng. Mater.* **2015**, *71*, 619–640. [CrossRef] [PubMed]
34. Ley, M.B.; Jørgensen, M.; Cerny, R.; Filinchuk, Y.; Jensen, T.R. From $M(BH_4)_3$ (M = La, Ce) Borohydride Frameworks to Controllable Synthesis of Porous Hydrides and Ion Conductors. *Inorg. Chem.* **2016**, *55*, 9748–9756. [CrossRef] [PubMed]
35. Sharma, M.; Didelot, E.; Spyratou, A.; Daku, L.M.L.; Cerny, R.; Hagemann, H. Halide Free $M(BH_4)_2$ (M = Sr, Ba, and Eu) Synthesis, Structure, and Decomposition. *Inorg. Chem.* **2016**, *55*, 7090–7097. [CrossRef] [PubMed]
36. Frommen, C.; Sørby, M.H.; Ravindran, P.; Vajeeston, P.; Fjellvåg, H.; Hauback, B.C. Synthesis, Crystal Structure, and Thermal Properties of the First Mixed-Metal and Anion-Substituted Rare Earth Borohydride $LiCe(BH_4)_3Cl$. *J. Phys. Chem. C* **2011**, *115*, 23591–23602. [CrossRef]
37. GharibDoust, S.P.; Brighi, M.; Sadikin, Y.; Ravnsbæk, D.B.; Cerny, R.; Skibsted, J.; Jensen, T.R. Synthesis, Structure, and Li-Ion Conductivity of $LiLa(BH_4)_3X$, X = Cl, Br, I. *J. Phys. Chem. C* **2017**, *121*, 19010–19021. [CrossRef]
38. Sadikin, Y.; Stare, K.; Schouwink, P.; Ley, M.B.; Jensen, T.R.; Meden, A.; Cerny, R. Alkali metal—Yttrium borohydrides: The link between coordination of small and large rare-earth. *J. Solid State Chem.* **2015**, *225*, 231–239. [CrossRef]
39. Hagemann, H.; Longhini, M.; Kaminski, J.W.; Wesolowski, T.A.; Cerny, R.; Penin, N.; Sørby, M.H.; Hauback, B.C.; Severa, G.; Jensen, C.M. $LiSc(BH_4)_4$: A novel salt of Li^+ and discrete $Sc(BH_4)_4{}^-$ complex anions. *J. Phys. Chem. A* **2008**, *112*, 7551–7555. [CrossRef] [PubMed]
40. Jaroń, T.; Wegner, W.; Fijałkowski, K.J.; Leszczyński, P.J.; Grochala, W. Facile Formation of Thermodynamically Unstable Novel Borohydride Materials by a Wet Chemistry Route. *Chem. A Eur. J.* **2015**, *21*, 5689–5692. [CrossRef] [PubMed]
41. Cerny, R.; Severa, G.; Ravnsbæk, D.B.; Filinchuk, Y.; D'Anna, V.; Hagemann, H.; Haase, D.; Jensen, C.M.; Jensen, T.R. $NaSc(BH_4)_4$: A Novel Scandium-Based Borohydride. *J. Phys. Chem. C* **2010**, *114*, 1357–1364. [CrossRef]
42. GharibDoust, S.H.P.; Ravnsbæk, D.B.; Cerny, R.; Jensen, T.R. Synthesis, structure and properties of bimetallic sodium rare-earth (RE) borohydrides, $NaRE(BH_4)_4$, RE = Ce, Pr, Er or Gd. *Dalton Trans.* **2017**, *46*, 13421–13431. [CrossRef] [PubMed]
43. Jaroń, T.; Grochala, W. Probing Lewis acidity of $Y(BH_4)(3)$ via its reactions with MBH_4 (M = Li, Na, K, NMe_4). *Dalton Trans.* **2011**, *40*, 12808–12817. [CrossRef] [PubMed]
44. Heere, M.; GharibDoust, S.H.P.; Sørby, M.H.; Frommen, C.; Jensen, T.R.; Hauback, B.C. In situ investigations of bimetallic potassium erbium borohydride. *Int. J. Hydrogen Energy* **2017**, *42*, 22468–22474. [CrossRef]
45. Wegner, W.; Jaroń, T.; Grochala, W. $MYb(BH_4)_4$ (M = K, Na) from laboratory X-ray powder data. *Acta Crystallogr. Sect. C Cryst. Struct. Commun.* **2013**, *69*, 1289–1291. [CrossRef] [PubMed]

46. Cerny, R.; Ravnsbæk, D.B.; Severa, G.; Filinchuk, Y.; D' Anna, V.; Hagemann, H.; Haase, D.; Skibsted, J.; Jensen, C.M.; Jensen, T.R. Structure and Characterization of $KSc(BH_4)_4$. *J. Phys. Chem. C* **2010**, *114*, 19540–19549. [CrossRef]
47. Aeberhard, P.C.; Refson, K.; Edwards, P.P.; David, W.I.F. High-pressure crystal structure prediction of calcium borohydride using density functional theory. *Phys. Rev. B* **2011**, *83*, 174102. [CrossRef]
48. Brighi, M.; Schouwink, P.; Sadikin, Y.; Cerny, R. Fast ion conduction in garnet-type metal borohydrides $Li_3K_3Ce_2(BH_4)_{12}$ and $Li_3K_3La_2(BH_4)_{12}$. *J. Alloys Compd.* **2016**, *662*, 388–395. [CrossRef]
49. GharibDoust, S.H.P.; Heere, M.; Sørby, M.H.; Ley, M.B.; Ravnsbæk, D.B.; Hauback, B.C.; Cerny, R.; Jensen, T.R. Synthesis, structure and properties of new bimetallic sodium and potassium lanthanum borohydrides. *Dalton Trans.* **2016**, *45*, 19002–19011. [CrossRef] [PubMed]
50. Jaroń, T.; Wegner, W.; Grochala, W. M $Y(BH_4)_4$ and $M_2LiY(BH_4)_{6-x}Cl_x$ (M = Rb, Cs): New borohydride derivatives of yttrium and their hydrogen storage properties. *Dalton Trans.* **2013**, *42*, 6886–6893. [CrossRef] [PubMed]
51. Møller, K.T.; Jørgensen, M.; Fogh, A.S.; Jensen, T.R. Perovskite alkali metal samarium borohydrides: Crystal structures and thermal decomposition. *Dalton Trans.* **2017**, *46*, 11905–11912. [CrossRef] [PubMed]
52. Schouwink, P.; Didelot, E.; Lee, Y.S.; Mazet, T.; Cerny, R. Structural and magnetocaloric properties of novel gadolinium borohydrides. *J. Alloys Compd.* **2016**, *664*, 378–384. [CrossRef]
53. Schouwink, P.; Ley, M.B.; Tissot, A.; Hagemann, H.; Jensen, T.R.; Smrcok, L.; Cerny, R. Structure and properties of complex hydride perovskite materials. *Nat. Commun.* **2014**, *5*, 5706. [CrossRef] [PubMed]
54. Dai, J.H.; Chen, Y.Y.; Xie, R.W.; Hu, Z.; Song, Y. Influence of alloying elements on the stability and dehydrogenation properties on $Y(BH_4)_3$ by first principles calculations. *Int. J. Hydrogen Energy* **2016**, *41*, 1662–1671. [CrossRef]
55. Remhof, A.; Borgschulte, A.; Friedrichs, O.; Mauron, P.; Yan, Y.; Züttel, A. Solvent-free synthesis and decomposition of $Y(BH_4)_3$. *Scr. Mater.* **2012**, *66*, 280–283. [CrossRef]
56. Park, K.; Lee, H.S.; Remhof, A.; Lee, Y.S.; Yan, Y.G.; Kim, M.Y.; Kim, S.J.; Züttel, A.; Cho, Y.W. Thermal properties of $Y(BH_4)_3$ synthesized via two different methods. *Int. J. Hydrogen Energy* **2013**, *38*, 9263–9270. [CrossRef]
57. Riktor, M.D.; Filinchuk, Y.; Vajeeston, P.; Bardaji, E.G.; Fichtner, M.; Fjellvåg, H.; Sørby, M.H.; Hauback, B.C. The crystal structure of the first borohydride borate, $Ca_3(BD_4)_3(BO_3)$. *J. Mater. Chem.* **2011**, *21*, 7188–7193. [CrossRef]
58. Schrauzer, G.N. Ermittlung des Ionencharakters mit Hilfe der Stabilitatsquotiententheoriet. *Naturwissenschaften* **1955**, *42*, 43.
59. Schrauzer, G.N. Die chemische Bestimmung des Ionencharakters im Lithiumborhydridt. *Naturwissenschaften* **1955**, *42*, 43–44.
60. Ley, M.B.; Paskevicius, M.; Schouwink, P.; Richter, B.; Sheppard, D.A.; Buckley, C.E.; Jensen, T.R. Novel solvates $M(BH_4)_3S(CH_3)_2$ and properties of halide-free $M(BH_4)_3$ (M = Y or Gd). *Dalton Trans.* **2014**, *43*, 13333–13342. [CrossRef] [PubMed]
61. Mauron, P.; Buchter, F.; Friedrichs, O.; Remhof, A.; Bielmann, M.; Zwicky, C.N.; Züttel, A. Stability and reversibility of $LiBH_4$. *J. Phys. Chem. B* **2008**, *112*, 906–910. [CrossRef] [PubMed]
62. Vajo, J.J.; Skeith, S.L.; Mertens, F. Reversible storage of hydrogen in destabilized $LiBH_4$. *J. Phys. Chem. B* **2005**, *109*, 3719–3722. [CrossRef] [PubMed]
63. Bosenberg, U.; Doppiu, S.; Mosegaard, L.; Barkhordarian, G.; Eigen, N.; Borgschulte, A.; Jensen, T.R.; Cerenius, Y.; Gutfleisch, O.; Klassen, T.; et al. Hydrogen sorption properties of MgH_2-$LiBH_4$ composites. *Acta Mater.* **2007**, *55*, 3951–3958. [CrossRef]
64. Lim, J.H.; Shim, J.H.; Lee, Y.S.; Suh, J.Y.; Cho, Y.W.; Lee, J. Rehydrogenation and cycle studies of $LiBH_4$-CaH_2 composite. *Int. J. Hydrogen Energy* **2010**, *35*, 6578–6582. [CrossRef]
65. Jin, S.A.; Lee, Y.S.; Shim, J.H.; Cho, Y.W. Reversible hydrogen storage in $LiBH_4$-MH_2 (M = Ce, Ca) composites. *J. Phys. Chem. C* **2008**, *112*, 9520–9524. [CrossRef]
66. Gennari, F.C. Destabilization of $LiBH_4$ by MH_2 (M = Ce, La) for hydrogen storage: Nanostructural effects on the hydrogen sorption kinetics. *Int. J. Hydrogen Energy* **2011**, *36*, 15231–15238. [CrossRef]
67. Jin, S.A.; Shim, J.H.; Cho, Y.W.; Yi, K.W.; Zabara, O.; Fichtner, M. Reversible hydrogen storage in $LiBH_4$-Al-LiH composite powder. *Scr. Mater.* **2008**, *58*, 963–965. [CrossRef]

68. Zhang, Y.; Tian, Q.F.; Zhang, J.; Liu, S.S.; Sun, L.X. The Dehydrogenation Reactions and Kinetics of 2$LiBH_4$-Al Composite. *J. Phys. Chem. C* **2009**, *113*, 18424–18430. [CrossRef]
69. Vajo, J.J.; Salguero, T.T.; Gross, A.E.; Skeith, S.L.; Olson, G.L. Thermodynamic destabilization and reaction kinetics in light metal hydride systems. *J. Alloys Compd.* **2007**, *446*, 409–414. [CrossRef]
70. Au, M.; Jurgensen, A.R.; Spencer, W.A.; Anton, D.L.; Pinkerton, F.E.; Hwang, S.J.; Kim, C.; Bowman, R.C. Stability and Reversibility of Lithium Borohydrides Doped by Metal Halides and Hydrides. *J. Phys. Chem. C* **2008**, *112*, 18661–18671. [CrossRef]
71. Zhang, B.J.; Liu, B.H. Hydrogen desorption from $LiBH_4$ destabilized by chlorides of transition metal Fe, Co, and Ni. *Int. J. Hydrogen Energy* **2010**, *35*, 7288–7294. [CrossRef]
72. Frommen, C.; Heere, M.; Riktor, M.D.; Sørby, M.H.; Hauback, B.C. Hydrogen storage properties of rare earth (RE) borohydrides (RE = La, Er) in composite mixtures with $LiBH_4$ and LiH. *J. Alloys Compd.* **2015**, *645*, S155–S159. [CrossRef]
73. Heere, M.; GharibDoust, S.H.P.; Brighi, M.; Frommen, C.; Sørby, M.H.; Cerny, R.; Jensen, T.R.; Hauback, B.C. Hydrogen Sorption in Erbium Borohydride Composite Mixtures with $LiBH_4$ and/or LiH. *Inorganics* **2017**, *5*, 31. [CrossRef]
74. Gennari, F.C. Mechanochemical synthesis of erbium borohydride: Polymorphism, thermal decomposition and hydrogen storage. *J. Alloys Compd.* **2013**, *581*, 192–195. [CrossRef]
75. Barkhordarian, G.; Klassen, T.; Dornheim, M.; Bormann, R. Unexpected kinetic effect of MgB_2 in reactive hydride composites containing complex borohydrides. *J. Alloys Compd.* **2007**, *440*, L18–L21. [CrossRef]
76. Dhliwayo, T. Development of advanced shield systems for fast neutrons. *Int. Nuclear Saf. J.* **2014**, *3*, 49–53.
77. Fantidis, J.G. The comparison between simple and advanced shielding materials for the shield of portable neutron sources. *Int. J. Radiat. Res.* **2015**, *13*, 287–295.